

1 **Democratizing macroecology: integrating unoccupied aerial systems**
2 **with the National Ecological Observatory Network**

3 Michael J. Koontz^{1*}, Victoria M. Scholl^{3,2,1}, Anna I. Spiers^{1,4}, Megan E. Cattau⁵, John Adler^{2,6},
4 Joseph McGlinchy^{1,7}, Tristan Goulden⁶, Brett A. Melbourne⁴, Jennifer K. Balch^{1,2}

5 ¹Earth Lab, University of Colorado; Boulder, CO, USA

6 ²Department of Geography, University of Colorado; Boulder, CO, USA

7 ³U.S. Geological Survey, Geosciences and Environmental Change Science Center; Lakewood,
8 CO, USA

9 ⁴Department of Ecology and Evolutionary Biology, University of Colorado; Boulder, CO, USA

10 ⁵Department of Human-Environment Systems, Boise State University; Boise, ID, USA

11 ⁶Battelle, National Ecological Observatory Network (NEON); Boulder, CO, USA

12 ⁷Hydrosat Inc., Washington, DC 20036, USA

13 **Correspondence:* mikoontz@gmail.com

14 *Keywords:* NEON, macroecology, UAS, drone

15 Date report generated: April 03, 2022

16 Open Research Statement: All data and code required to reproduce the analysis and the
17 workflow presented in this manuscript can be found on the Open Science Framework at
18 <https://doi.org/10.17605/OSF.IO/ENBWU> and on GitHub at
19 <https://github.com/mikoontz/neon-drone-workflow>.

20 **Abstract**

21 Macroecology research seeks to understand ecological phenomena with causes and
22 consequences that accumulate, interact, and emerge across scales spanning several orders
23 of magnitude. Broad-extent, fine-grain (i.e., high spatial resolution) information is needed
24 to adequately capture these cross-scale phenomena, but these data are costly to acquire
25 and process. Unoccupied aerial systems (UAS, or drones carrying a sensor payload) and the
26 National Ecological Observatory Network (NEON) make the broad-extent, fine-grain
27 observational domain more accessible to researchers by lowering costs and reducing the
28 need for highly specialized equipment. Integration of these tools can further democratize
29 macroecological research, as their strengths and weaknesses are complementary. However,
30 using these tools for macroecology can be challenging because mental models are lacking,
31 thus requiring large upfront investments in time, energy, and creativity to become
32 proficient. This challenge inspired a working group of UAS-using academic ecologists,
33 NEON professionals, imaging scientists, remote sensing specialists, and aeronautical
34 engineers at the 2019 NEON Science Summit in Boulder, Colorado, to synthesize current
35 knowledge on how to use UAS with NEON into a mental model for an intended audience of
36 ecologists new to these tools. Specifically, we provide (1) a collection of core principles for
37 collecting high-quality UAS data for NEON integration and (2) a case study illustrating a
38 sample workflow for processing UAS data into meaningful ecological information and
39 integrating it with NEON data collected on the ground with the Terrestrial Observation
40 System and remotely from the Airborne Observation Platform. With this mental model, we

41 advance the democratization of macroecology by making a key observational domain– the
42 broad-extent, fine-grain domain– more accessible via NEON/UAS integration.

43 **Introduction**

44 Macroecology is the study of spatially extensive systems whose biological, geophysical, and
45 social components interact dynamically both within and across spatiotemporal scales
46 (Heffernan et al. 2014). Macroecology, in its explicit consideration of scale, extends from a
47 rich history of basic ecological research seeking to explain patterns in nature (Turner 1989,
48 Levin 1992). At the same time, macroecology is highly relevant to applied ecology, as the
49 broader spatial extents studied reflect the scale at which many societally relevant
50 challenges, and perhaps their solutions, arise (Heffernan et al. 2014, LaRue et al. 2021). The
51 causes and consequences of phenomena under investigation in macroecology can span
52 many spatial scales, which motivates a characteristic feature of the data to be brought to
53 bear: they must often be simultaneously fine in grain (i.e., spatial resolution) and broad in
54 extent (Beck et al. 2012).

55 Ecologists typically face a data collection tradeoff between grain and extent that constrains
56 the observational domain of their research (Ernest 2018, Estes et al. 2018). Indeed, the
57 spatial and temporal observational domains of most ecology research are narrow (Estes et
58 al. 2018). The grain/extent tradeoff can sometimes be overcome, but at a high cost. For
59 example, the Global Airborne Observatory collects high spatial and spectral resolution data
60 at broad extents (Asner et al. 2007, Asner et al. 2012), but the price of data acquisition and
61 processing tallies in the millions of US dollars (USD), even though the per-area cost is low

62 (Asner et al. 2013). As another example, the US Forest Service Forest Inventory and
63 Analysis program maintains a regular network of over 350,000 fine-grain field plots
64 regularly spaced over the entire forested area of the United States (over 9.1 million km²;
65 approximately 1 plot every 2400 hectares) at an annual cost of tens of millions of dollars
66 (Gillespie 1999, Alvarez 2020). Most science studies have relatively modest budgets and
67 are conducted by just a few individuals (Heidorn 2008). The modal award size from the
68 National Science Foundation's (NSF) Division of Environmental Biology was about
69 \$200,000 USD between 2005 and 2010 (Hampton et al. 2013). While the fine-grain, broad-
70 extent observational domain is invaluable for macroecology, it can be inaccessible to
71 ecologists with resource or funding limitations.

72 Macroecology can be democratized when barriers to research participation are reduced
73 (Guston 2004), such as by innovating past limitations to or lowering the cost of access to
74 relevant scales of observation. Removing these barriers improves science because the rate,
75 direction, and quality of science are, in part, shaped by the available research inputs
76 (Nagaraj et al. 2020). For instance, the cost of imagery from the archive of Landsat earth
77 observation imagery was reduced in 1995 and restrictions on sharing were relaxed, which
78 dramatically increased the quantity, quality, and diversity of Landsat-enabled science
79 (Nagaraj et al. 2020). The same archive became freely available in 2008 with concomitant
80 benefits to projects that rely on Landsat observations (e.g., Picotte et al. 2020). The
81 changing accessibility of Landsat data is noteworthy for macroecology, as the archive
82 provides consistent global-extent, relatively fine-grain (30 meter) imagery since 1984.
83 Particularly when integrated with other tools whose purpose is to broaden research
84 participation (such as the free, planetary-scale geographic information system "for

85 everyone," Google Earth Engine; Gorelick et al. 2017), Landsat imagery has led to
86 breakthrough science that is "globally consistent and locally relevant" such as the first
87 global map of forest cover changes over a decade-long period at a relatively fine scale
88 (Hansen et al. 2013). Thus, democratized research stimulates revolutionary science.

89 In its democratic aim, the National Ecological Observatory Network (NEON) is
90 revolutionary (NSF 2013, Balch et al. 2020). NEON is a continental-scale observation
91 facility in the United States comprising 81 sites within 20 ecologically distinct domains
92 and an operational lifespan on the order of decades (Keller et al. 2008, Schimel 2013).
93 NEON is designed to collect rigorous, consistent, long-term, and open access data to better
94 understand how US ecosystems are changing, using a combination of field measurements
95 obtained by trained personnel, ground- and aquatic-based automated sensors, and plane-
96 based instruments that collect both active and passive remotely-sensed data (Kampe et al.
97 2010, NSF 2013). NEON observations span spatial scales, from measurements of individual
98 organisms within small field plots to 10 cm resolution red-green-blue (RGB) imagery and 1
99 m hyperspectral and lidar imagery across hundreds of square kilometers, with
100 measurements replicated across sites that span the continental extent of NEON (Keller et
101 al. 2008). A stated goal of NEON is to democratize access to ecological research, particularly
102 at broad extents (NSF 2013)- its promise is continental-scale ecology for everyone. NEON
103 pairs publicly available data with a strong outreach and education effort to help realize this
104 promise. In this way, NEON broadens access to macroecology by reducing barriers to entry,
105 particularly cost, fieldwork requirements, and technical expertise (Nagy et al. 2021). An
106 "instrument" like NEON collecting standardized data at such scales leads to inevitable
107 tradeoffs- in the specific times, locations, and type of data that are sampled. While the

108 NEON data are on their own sufficient for advancing ecology, part of what makes NEON
109 revolutionary is its foresight in facilitating connections to other ecological data. In this way,
110 the fundamental limitations of NEON can be overcome with bridges to more targeted
111 ecological studies.

112 Unoccupied aerial systems (UAS) can also revolutionize ecology (Anderson and Gaston
113 2013). UAS, comprising a vehicle and a payload, are increasingly being used to collect high
114 spatial resolution information over relatively large spatial extents for ecological science
115 applications (Wyngaard et al. 2019). The vehicle is also known as a “drone” or a “UAV”
116 standing for “unoccupied aerial vehicle,” “unhumanned aerial vehicle,” “uncrewed aerial
117 vehicle,” or “unmanned aerial vehicle,” though we support phasing out the gendered
118 language of this last expansion (Joyce et al. 2021). The payload is the instrumentation
119 carried by the vehicle beyond what is critical for flight operations, and gives the UAS its
120 scientific value. Importantly, it isn’t the vehicle itself that enables ecological studies at
121 heretofore inaccessible scales, but rather the vehicle’s ability to position a data collecting
122 payload (i.e., a sensor) in a repeatable, efficient, hard-to-reach manner. For example, one
123 use case for UAS is structure from motion (SfM) photogrammetry which generates a 3-
124 dimensional model of an area of interest using 2-dimensional images from multiple
125 overlapping viewing angles (Westoby et al. 2012). The minimum requirement for SfM
126 photogrammetry is 2-dimensional imagery, which can be captured from the ground using a
127 hand-held sensor (e.g., a digital camera) to great effect for some applications (Piermattei et
128 al. 2019). A UAS-based camera can capture imagery from higher up in, or above, the
129 canopy, which allows for measurement of higher vegetation strata (Kuželka and Surový
130 2018), including total height for above-canopy applications. UAS-based SfM

131 photogrammetry also increases the extent that can be covered with surveys (Jackson et al.
132 2020) because aerial transects are unimpeded by varied terrain and vegetation
133 encountered on ground transects. Unimpeded aerial transects are also more reliably
134 repeated than ground surveys that require navigating through vegetation and are likely to
135 be less impactful to that vegetation. UAS provide an avenue to flexibly and affordably fill
136 spatiotemporal gaps in data collected by traditional means- they can be deployed more
137 frequently and capture finer grain data than airplane- and satellite-based platforms, and
138 can cover greater extents than ground surveys.

139 UAS and NEON complement each other. Each can be a key tool for macroecology research,
140 but their integration offers an opportunity to alleviate some of their fundamental
141 constraints in a similar way as integration of NEON with other earth observing networks
142 (Balch et al. 2020, Nagy et al. 2021). NEON data derive from “state of the science”
143 instrumentation with thorough documentation, and are standardized at a continental scale.
144 NEON data collection is pre-planned, which makes the resulting data somewhat
145 predictable, but also rigid in space, time, and type. On the other hand, UAS operations are
146 nimble and customizable, but the resulting data are relatively under-validated with data
147 standards that are ad-hoc, idiosyncratic, and lacking in a consistency which makes
148 interoperability of those data across projects a challenge (Wyngaard et al. 2019).
149 Realization of the benefits of UAS-NEON integration by ecologists is dually challenged by
150 the relative novelty of these tools (Wyngaard et al. 2019, Nagy et al. 2021) as well as by a
151 community gap in the data science skills needed to navigate their associated workflows
152 (Hampton et al. 2017, Balch et al. 2020, Nagy et al. 2021). Not knowing where to start with
153 two new tools is a daunting proposition, and unstructured efforts to gain practical

154 proficiency for research often comes at the expense of doing research itself (Olah and
155 Carter 2017). Reducing these barriers to proficiency therefore has tremendous research
156 value.

157 Mental models help novices become experienced practitioners by providing a contextual
158 framework for new knowledge (Knapp and D'Avanzo 2010). A lack of a synthesized
159 contextual framework for practical use of UAS for ecology research, particularly for NEON
160 integration, challenges adoption of these tools and hampers their ability to democratize
161 macroecology (Wyngaard et al. 2019, Assmann et al. 2019). We assembled a working group
162 of participants at the 2019 NEON Science Summit in Boulder, Colorado with a goal to
163 synthesize current practical knowledge and provide a sample workflow to guide ecologists
164 with a mental model for using UAS and integrating with NEON. In this work, we aim to
165 lower the barrier to entry for using UAS and NEON to do ecology. Specifically, we focus on
166 optical data collected by each tool over terrestrial sites and provide (1) a collection of what
167 we consider to be the ten core principles for integrating UAS with NEON (science
168 requirements, vehicle, payload, environment, flight planning, rules/regulations,
169 radiometric calibration, georeferencing, data management, and data processing) and (2) an
170 illustration of these principles with a real-world, well-documented workflow that
171 processes UAS data into meaningful ecological information, then integrates it with NEON
172 Airborne Observation Platform (AOP) and Terrestrial Observation System (TOS) data at the
173 NEON Niwot Ridge (NIWO) site.

174 **Core principles for UAS/NEON integration**

175 **Science requirements**

176 We support and extend one of Assmann et al. (2019)'s themes regarding research use of
177 UAS in order to highlight the first core principle for integrating UAS with NEON: knowing
178 what the science requirements are for the data to be collected and what data collection
179 efforts are "good enough" to meet those requirements. Using NEON to advance ecology is a
180 type of data-driven discovery, in which the high-quality, but rote data collection occurs
181 before the science questions are generated (Lindenmayer and Likens 2018). UAS data
182 collection can be more flexible and responsive, which makes it more suitable for discovery
183 driven by particular questions posed ahead of time. Integration of UAS and NEON could
184 therefore be considered a hybrid between data- and question-driven discovery, where
185 there is a dynamic between creative use of the existing NEON data, generation of new
186 specific questions, and augmentation of the existing NEON data with UAS data collection to
187 help answer those questions. During this process, a clear science question helps guide the
188 data collection/collation needs, which can minimize the amount of researcher energy spent
189 on developing tools and workflows that ultimately prove to be superfluous (Joseph et al.
190 2021).

191 **Vehicle**

192 The vehicle in a UAS is the flying machine that holds the payload. One key distinction
193 between vehicle types is whether rotor systems or fixed wings are used for lift (the upward
194 force that keeps the vehicle in the air). Rotocopter vehicles (also known as "multicopters,"

195 “multirotors,” “quadcopters,” “hexacopters,” or “octocopters” depending on the number of
196 rotor systems) consist of a body and 4-8 rotary systems that provide both lift and thrust
197 (horizontal motion). These types of vehicles are characterized as “vertical takeoff and
198 landing” (VTOL). Fixed wing aircraft use wings for lift, and use rotor systems only for
199 thrust. Hybrid vehicles use rotor systems for lift during ascent and descent, but fixed wings
200 for lift during flight and are sometimes referred to as VTOL fixed wing systems to highlight
201 this combination of features. The structure and size of the vehicle determine its
202 functionality in the field and thus a project’s objectives can often help constrain the choices
203 available. Rotocopter platforms are more maneuverable, often less expensive, easier to fly,
204 more transportable, and have a higher payload capacity relative to fixed wing aircraft. For
205 these reasons, rotocopters are often preferred by ecologists. On the other hand, fixed wing
206 aircraft have longer flight times with better battery usage and thus can cover larger areas
207 more efficiently than rotocopters. For example, covering the full extent of a given AOP
208 footprint ($147.6 +/- 107.2 \text{ km}^2$ for core and relocatable sites) may be most efficiently
209 conducted with a fixed-wing or hybrid vehicle. They are also more stable in adverse
210 conditions (e.g., high winds) and have a safer recovery from motor power loss. VTOL fixed
211 wing systems can combine the efficiency of a fixed wing with the small takeoff/landing
212 footprint of a rotocopter. A summary of the advantages and disadvantages of these vehicle
213 types is found in Table 1.

214 A flat surface clear of obstructions (e.g., on dirt rather than grass, away from forest canopy)
215 is ideal for UAS takeoffs and landings. VTOL systems require a smaller takeoff and landing
216 footprint, which may be satisfied with only a small canopy gap, compared to vehicles that
217 use fixed wings for lift, which require a “runway” for fixed wing vehicles. Locating such a

218 site may be challenging at some NEON sites (e.g., NIWO, with dense canopy cover) and easy
219 at others (e.g., SJER, with an open woodland ecotype). Takeoffs and landings from a clean,
220 stable, flat surface (e.g., plywood, car floor mat) will prevent dirt from obstructing or
221 scratching the sensor lens, and will make for a more controlled ascent/descent.

222 With any platform, vehicle endurance limitations and the mission goals will determine how
223 many flights are required to complete data collection. In many cases, it will be necessary to
224 purchase several batteries to keep the vehicle flying for the duration of a field day. Even if
225 only one flight is needed to collect data, extra batteries are still valuable to have on hand in
226 case the first flight doesn't go as planned and follow-up flights are required. An energy
227 source to charge batteries in the field, like a solar charger or gasoline-powered generator,
228 may also be necessary for very long missions or multiple days of data collection. As a
229 guideline, you can determine how many batteries your portable energy source can charge
230 by determining its energy capacity in watt-hours (Wh), multiplying by 90% (making the
231 calculation such that you leave 10% of the capacity rather than fully draining it), then
232 dividing by the capacity of a single UAS battery in watt-hours and rounding down to the
233 nearest whole number to account for any unpredictable inefficiencies. For instance, a Goal
234 Zero Yeti 1400 battery (used successfully by some authors) can be charged with solar
235 panels and stores 1,400 Wh of energy, which results in 1,260 Wh of usable energy if it were
236 to be drained to 10% capacity. Each TB48 battery of the DJI Matrice 100 aircraft stores
237 about 130 Wh of energy, so the Yeti 1400 should be able to charge about nine batteries
238 before it needs to be recharged itself ($1,260 / 130 = 9.7$, which is 9 when rounded down). If
239 an efficient one-gallon, gasoline-powered generator can produce 6,000 Wh of energy, that

240 results in 5,400 Wh of usable energy which is equivalent to charging about 41 batteries for
241 the Matrice 100.

242 **Payload**

243 The payload is the equipment carried by the UAS that collects data and combines with the
244 vehicle to constitute the system (the “S” in “UAS”). In fact, despite the typical focus on the
245 drone vehicle, the payload component is at least as important, since the main purpose of
246 the vehicle is merely to position the payload where it needs to be in order to capture
247 appropriate data. For ecologists interested in optical data, the payload may be a simple
248 camera or a more specialized remote sensing sensor sensitive to particular wavelengths of
249 electromagnetic radiation. The scientific questions will dictate the data requirements,
250 which will in turn drive the payload decision. Typically, the selection of a sensor represents
251 a trade-off between spatial resolution (the size of pixels in the imagery at a set altitude),
252 spectral resolution (the number of distinct portions of the electromagnetic spectrum that
253 the sensor can detect), spectral extent (how much of the electromagnetic spectrum the
254 sensor can detect), and cost. For example, while hyperspectral data provide high spectral
255 resolution and extent that may allow measurement of specific chemical compounds in
256 vegetation (e.g., foliar nitrogen; Knyazikhin et al. 2013), a multispectral instrument with
257 fewer spectral channels (Koontz et al. 2021) or even an RGB camera (Scholl et al. 2020)
258 may be more than sufficient for classifying vegetation to species. Similarly, sensors with
259 high spatial resolution can capture fine detail in their imagery but may reduce the ability to
260 measure a variable of interest, such as individual trees, as post-processing steps can be
261 negatively affected by the movement of those fine details in the wind (Young et al. 2021).

262 Hyperspectral instruments and high resolution cameras are relatively expensive in terms
263 of purchase cost, post-processing time, and data storage requirements, but simple RGB and
264 multispectral cameras can be affordably bought off-the-shelf so it is worth considering
265 whether they would suffice for the scientific question of interest. A summary of the
266 advantages and disadvantages of these different payload types for collecting optical data
267 can be found in Table 1.

268 It is also important to consider how the payload will be integrated with the vehicle, which
269 generally requires considering the combination of the vehicle and payload simultaneously.
270 In some cases, the payload can operate entirely independently from the vehicle, and
271 integration only requires a means of physically attaching the components together. In other
272 cases, the payload relies both on power and electronic signaling from the vehicle in order
273 to capture data, and integration may require more specialized electrical and mechanical
274 engineering expertise. It's generally advisable to use a pre-built integration kit or an
275 already-integrated sensor/vehicle system if the payload meets the science requirements
276 (or nearly so).

277 **Environment**

278 The environment of the UAS mission can affect both the equipment performance and the
279 data collection such that the intended operation conditions must be considered during
280 vehicle/payload selection and flight planning. Foremost, the vehicle and the payload must
281 be capable of functioning in the desired environment. UAS flights at high elevations or in
282 cold weather will drain battery faster than at sea level, and some popular vehicles won't
283 allow takeoff if the temperature is too cold (or hot). While some vehicles are designed to

284 withstand light precipitation and dust, many would be damaged under such flight
285 conditions. Heavy winds can push the UAS off-course or require the UAS to work harder to
286 maintain its course, which drains battery faster and reduces endurance. Variable terrain
287 within the survey area may also affect vehicle endurance, as more energy is required to
288 ascend and descend while also traversing along flight transects in the horizontal plane.
289 Managing the temperature of the mission critical electronics is just as important as that of
290 the vehicle's batteries during UAS operations. The vehicle remote controller and any other
291 peripherals such as a tablet computer are susceptible to battery drain in extreme
292 temperatures, and cold temperature can cause the vehicle and/or sensor to malfunction.
293 The mean annual temperature for NEON AOP sites ranges from -12°C at the Utqiāgvik site
294 in Alaska to 25°C at Lajas Experimental Station in Puerto Rico (NEON Field Site Metadata;
295 https://www.neonscience.org/sites/default/files/NEON_Field_Site_Metadata_20210226_0.csv; accessed 2021-03-16). Expectations of unfavorable environmental conditions may be
296 enough to dictate what equipment should comprise the UAS. For example, high-wind
297 conditions at NIWO may warrant a fixed wing platform; however, the dense forest would
298 make takeoff and landing much easier with a rotocopter. In some cases, steps can be taken
300 to mitigate the unfavorable environmental conditions, such as keeping equipment out of
301 direct sunlight to prevent overheating (to the point of adding sun umbrellas or shade tarps
302 to the required equipment list) and storing batteries in a dry cooler when not in use in
303 order to insulate them against temperature extremes.
304 Environmental conditions may also impact data collection on automated flights,
305 particularly for optical data. Ideal conditions for optical data collection are evenly lit with
306 either complete cloud cover or clear skies. If flying takes place under clear sky conditions,

307 then the sun should be high in the sky so it doesn't cast long shadows- ideally within a
308 couple of hours of solar noon (i.e., 10am and 2pm for standard time, and 11am to 3pm for
309 regions that observe daylight savings time) (Assmann et al. 2019). Note that some SfM
310 software guidelines specifically suggest *not* flying near solar noon, as this can create
311 particularly bright areas within each image that challenges the SfM algorithms
312 (MapsMadeEasy; https://www.mapsmadeeasy.com/data_collection; accessed 2021-11-
313 19).

314 Prior to flights, it is important to ensure that weather will be favorable for data collection. A
315 handheld instrument for measuring temperature, relative humidity, and wind speed may
316 also aid in the reporting of flight conditions, though note that the wind speed at flight
317 altitude may be different than what is measured on the ground. In many cases, taking a
318 picture of the sky and a screenshot of the weather forecast from a reputable source (e.g.,
319 the National Oceanic and Atmospheric Administration) is a convenient and sufficient way
320 to ensure later reporting on flight conditions. In fact, the NEON AOP does exactly this for
321 their daily flight reports.

322 **Flight planning**

323 One of the key benefits of UAS operations is the ability to program missions to be
324 automatically followed by the vehicle's onboard flight software. For optical data collection
325 such as that required for SfM photogrammetry, the mission typically involves aerial
326 transects with images captured at regular time or distance intervals so that objects in a
327 scene are imaged from many viewing angles (often in excess of 100; Figure 1). Successful

328 flight planning requires consideration of the flight parameters, flight planning software,
329 and operation routine.

330 The flight parameters are crucial determinants of whether or not the SfM photogrammetry
331 will successfully create a digital model of the survey area. Flight parameters are typically
332 described in terms of the front and side overlap of the resulting imagery, as well as the
333 sensor angle. The front overlap is a function of flight speed, flight altitude, frequency of
334 image capture, and the vertical field of view of the sensor, while the side overlap is a
335 function of flight altitude, horizontal field of view of the sensor, and distance between
336 transects. Overlap in excess of 80% for both front and side overlap (Dandois et al. 2015)
337 and even as high as 95% front overlap (Torres-Sánchez et al. 2018, Frey et al. 2018) is
338 required for successful photogrammetric reconstructions of more complex vegetation
339 (such as denser forests) using commonly available photo processing software. Lower
340 overlap may be sufficient for 2-D mapping quality, though the processed product may not
341 penetrate deeply into canopy gaps (Dandois et al. 2015) and image artifacts such as
342 “leaning” objects which were only imaged from an oblique angle are more prevalent.
343 Additional overlap can be achieved by augmenting parallel transects with a second set of
344 parallel transects rotated 90 degrees to the first (a cross hatch pattern; Figure 1).
345 Additional viewing angles can be achieved by tilting the sensor off nadir in order to capture
346 oblique imagery which can aid in scene reconstruction (James and Robson 2014, Cunliffe et
347 al. 2016). Published work exists that determines optimal flight parameters for creating
348 digital representations of specific survey areas (Dandois and Ellis 2013, Torres-Sánchez et
349 al. 2018, Frey et al. 2018, Ni et al. 2018, Nesbit and Hugenholtz 2019, Díaz et al. 2020,

350 Young et al. 2021, Swayze et al. 2021), but it still may require some trial and error (or a
351 new study) to optimize parameters for a new study area or system.

352 Flight planning is typically achieved using specialized software, sometimes run on a
353 separate device like a tablet computer. Most flight software allows for setting the altitude
354 as well as the desired forward and side overlap for a given aircraft and sensor. Two other
355 important software features that may routinely be relevant for ecology are terrain
356 following and internet-free operations. Terrain following enables the vehicle to ascend and
357 descend to match topographic changes within the area of interest, such that approximately
358 the same altitude above ground level is maintained throughout all aerial transects. This
359 serves two key functions: it ensures the safety of the vehicle and it maintains
360 approximately the same ground sampling distance for imagery which aids in processing.

361 Some missions are most easily created once in the field in order to incorporate better
362 information on the area of interest, takeoff/landing locations, and visibility throughout
363 flight. An ability for the software to function offline and to cache background map imagery
364 can be critical for real-world UAS use. Flight software is resource intensive and generally
365 requires a computer or tablet with relatively high computing power. We have experienced
366 flight software freezing mid-flight due to compute resource overload when using tablets
367 that weren't up to the task, which can create a hazardous situation. It is likely worth
368 investing in a device with faster processors and/or more RAM. Finally, some flight software
369 provide additional functionality if the tablet has geolocation services– an ability to
370 determine its location on Earth by connecting with satellite networks. For instance, the
371 flight software may display the tablet's location on the background map during flight or
372 even update the “home point” location for the UAS during the mission as the pilot moves

373 around. The home point is the location to which the UAS returns and lands after a mission
374 is completed, a battery is depleted, or the pilot triggers a manual “return to home”
375 command. An updating home point might allow the pilot to traverse the landscape to stay
376 closer to the UAS, thereby better maintaining visual line of sight or allowing the UAS to
377 collect more data per flight since the travel distance to the landing point is minimized
378 (during which time data typically aren’t collected). Not all tablets have geolocation
379 services; as of this writing, the Cellular+WiFi version of the Apple iPad Pro has geolocation
380 services, but the WiFi-only version does not.

381 A final consideration for successful flight planning is to create a routine for consistently
382 executing missions. Consistent repetition of routine steps prior to, during, and after a flight
383 ensures that all components of the UAS work as intended in concert with each other, and
384 checklists facilitate this consistency (Degani and Wiener 1993). We highly recommend
385 developing and using some kind of checklist for UAS operations (Supplementary
386 Information)– there is good reason they are part of standard operations for a range of
387 aviators from pilots of small private aircraft to NEON AOP to NASA astronauts! Some
388 applications (such as Kittyhawk; <https://kittyhawk.io/>) allow for automatic logging of
389 checklist run-throughs, which further reduces barriers to their use. For our mission, we
390 used Map Pilot for DJI by DronesMadeEasy, which enables full control of front/side overlap
391 and camera angle, as well as allows for crosshatch flight patterns, terrain following, and
392 caching of data for use in the field when an internet connection isn’t available.

393 **Regulations**

394 In the United States, research use of UAS must comply with legal regulations that govern
395 flight operations. These restrictions have historically been cited as a hurdle to adoption of
396 UAS for research use (Vincent et al. 2015). There are currently three main legal
397 frameworks governing UAS operations within the United States: permissions/regulations
398 for a specific organization (e.g., a university) granted under a Certificate of Authorization
399 (COA) from the Federal Aviation Administration (FAA), regulations for commercial
400 operations (described in Title 14 of the Code of Federal Regulations Part 107 and
401 colloquially referred to as “Part 107 rules”), and regulations for recreational operations
402 (described in Chapter 448 of Title 49, United States Code, Section 44809 and colloquially
403 referred to as “Recreational Flyer rules”). COAs are generally labor intensive to set up and
404 maintain, as they require ongoing coordination with the FAA, but they can allow for
405 operations not typically permitted under other regulatory frameworks. The commercial
406 and recreational operational rules apply to individuals, rather than organizations, and have
407 progressively become more clearly defined and permissive. For instance, a recent
408 amendment to the Part 107 regulations clarified that use of UAS by an institution of higher
409 education for research or education purposes is considered “recreational use,” and is
410 subject to recreational operations rules rather than commercial operations rules. These
411 rules applying to individuals allow for myriad opportunities to use UAS to collect ecological
412 data without the complex organizational overhead required for a COA. However, the rules
413 within each of these categories are still liable to change, and UAS pilots are responsible for
414 staying aware of any updates.

415 UAS pilots in the US must obtain some kind of credentials to operate UAS for research use.
416 Researchers flying under a COA would obtain credentials according to the rules specific to
417 their organization. Flying under Part 107 rules requires a “remote pilot certificate” from
418 the FAA, which can be obtained by passing an initial knowledge exam and expires after 2
419 years. Flying under Recreational Flyer rules requires a TRUST Certificate from the FAA,
420 which can be obtained by completing a Recreational UAS Safety Test that does not expire.
421 Unlike permissions granted under a COA, the Part 107 and TRUST credentials stay with the
422 pilot and are transferable if the pilot changes organizations (e.g., a graduate student can’t
423 operate a UAS for research under a university’s COA after they graduate, but they would
424 still retain their ability to operate with their FAA-granted credentials).

425 In general, there are some legal limits to the kinds of UAS flight operations allowed under
426 any regulatory framework. UAS pilots are responsible for ensuring that their equipment
427 and flight plan are in compliance with whichever regulatory framework they are operating
428 under. As with pilot credentials, researchers operating under a COA would need to comply
429 with the flight operations rules specific to their organization. Two of the most relevant
430 flight restrictions for ecologists operating under both Part 107 and Recreational Flyer rules
431 are: 1) the UAS must be within visual line-of-sight of the pilot in command (or within visual
432 line of sight of another crew member acting as a “visual observer” as long as that observer
433 has direct communication with the pilot in command), 2) the UAS must fly no higher than
434 400 feet (122 m) above ground level (AGL). Part 107 rules do constrain operations in other
435 specific ways, which may also apply to flights under Recreational Flyer rules that prohibit
436 unsafe operations. For instance, UAS can’t fly faster than 87 knots [161 km/h], UAS must be
437 at least 500 feet [152 m] below clouds and 2000 feet [609 m] horizontally from clouds.

438 However, high quality optical data collection usually requires UAS operations to be well
439 within these limits. Additional authorizations are needed to fly in “controlled” airspace (i.e.,
440 class B/C/D/E airspace, typically near airports), to fly a UAS above 55 lbs, and to fly a UAS
441 beyond line-of-sight. Some of these authorizations are relatively easy to obtain (e.g., many
442 requests to fly in controlled airspace below 400 feet (122 m) AGL can be automatically
443 granted in near real time using the Low Altitude Authorization and Notification Capability
444 (LAANC)), while others are nearly impossible (at the time of this writing) and are likely
445 beyond the reach of an ecological data collection campaign (e.g., beyond visual line-of-sight
446 flights). Finally, the drone itself may need to be marked and registered with the FAA. The
447 FAA website is usually the best source of the most up-to-date information about the rules
448 that might govern UAS research flights (<https://www.faa.gov/uas/>; accessed 2022-03-11).

449 It is important to connect with the appropriate land manager before flying on public land to
450 obtain appropriate site access if necessary, to check for temporary closures (e.g., bird
451 nesting), and to be a good neighbor. Because NEON does not own the land on which they
452 operate, flying NEON sites will require contacting and obtaining permission from the site
453 host; contact information is available on the NEON webpage for each site, and NEON staff
454 may also help facilitate those connections. Additional, non-NEON research is allowed at
455 some but not all sites. If permission is obtained, it is important not to disturb any existing
456 research being conducted at those sites, to maintain a 20m buffer around any NEON
457 distributed plot, and to completely avoid the area of the tower airshed (which is also
458 delineated on the NEON webpage for each site; e.g., <https://www.neonscience.org/data-samples/data/spatial-data-maps>). Clear communication with concerned parties of UAS
459 flights for research, even if there is every legal right to fly at a particular location, is
460

461 important for building community credibility and longevity for UAS as a tool for ecologists.
462 Finally, as with flight planning, it is best practice to develop a routine and a checklist (see
463 Supplementary Information) for determining whether UAS flights are allowed in the
464 intended survey area under the relevant regulatory framework.

465 **Radiometric calibration**

466 Optical data from UAS-mounted sensors must be radiometrically calibrated in order to
467 convert otherwise arbitrary image pixel values into meaningful, standardized units like
468 reflectance. Applying image preprocessing steps (e.g., correcting for camera artifacts such
469 as vignetting and dark noise) and subsequent radiometric calibration allows our UAS data
470 to be comparable with high-quality scientific data products derived from the NEON AOP.
471 The Empirical Line Method (ELM) has proved to be a simple and accurate UAS radiometric
472 calibration option (Wang and Myint 2015). ELM requires the placement of at least two
473 materials such as calibrated reflectance panels with known reflectance in the scene, which
474 are imaged while the sensor is in flight. These images containing the calibrated reflectance
475 panels are then used to translate image pixel values to reflectance for each spectral band
476 for the whole survey area. For some sensors, particularly low cost multispectral sensors
477 designed for agriculture, a downwelling light sensor (DLS a.k.a. sunshine sensor) also
478 records data about the illumination levels at the exact moment that each image is captured.
479 This information is often incorporated into the SfM processing to partially correct for
480 varying light conditions throughout the flight. Importantly, the DLS can help account for
481 varying illumination from image-to-image, but it doesn't allow for conversion of the image

482 pixel values into a standardized unit of reflectance the way that calibrated reflectance
483 panels can.

484 NEON implements a complex algorithm to convert its imaging spectrometer data to units of
485 reflectance (Karpowicz and Kampe 2015) that is founded on a similar principle as ELM. A
486 series of vicarious calibration flights are conducted with the NEON AOP before and after
487 every field season (Leisso et al. 2014). They fly over two large tarps with 48% (medium
488 gray) and 3% (black) reflectance, collect ground-based reflectance measurements of these
489 tarps with an ASD, and use these data to verify the radiometric calibration of the NEON
490 AOP Imaging Spectrometer (<https://www.neonscience.org/data-collection/imaging-spectrometer>). The reflectance of these tarps is meant to represent the upper and lower
491 bounds of reflectance typically seen in nature. NEON's algorithm also compensates for the
492 scattering and absorption of light as it travels through the atmosphere (e.g., haze, water
493 vapor) on its optical path to the AOP.

495 Using three panels with varying gray levels will allow for the most flexibility in calibration
496 methodology for UAS image data. Ideally, panels should be large enough to be imaged
497 during flight and contain an area of 10 x 10 pixels (Wang and Myint 2015). Panels should
498 be matte (as opposed to shiny or glossy) with a smooth, horizontal surface (Smith and
499 Milton 1999). Panel colors should be shades of black (near 0% reflectance) and gray,
500 ideally covering the range of reflectance for the subject of interest. White (near 100%
501 reflectance) panels are not recommended because they can saturate and cause other issues
502 (Cao et al. 2019). For plant surveys, we recommend a medium gray, dark gray, and black
503 target because vegetation tends to be about 50% average reflectance or medium gray.

504 Calibrated reflectance panels often come with the sensor to be integrated on the vehicle,
505 but they can also be purchased separately or made at home. Care must be taken with
506 homemade panels because, even though they may appear a particular shade to the human
507 eye (visible spectrum), they may not be a similar reflectance across all wavelengths
508 observed by a multi-spectral or hyperspectral sensor. Many studies have identified
509 promising materials for homemade panels: plywood covered with matte paint (Rosas et al.
510 2020), gray linoleum, and black fine-weave cotton fabric (Cao et al. 2019).

511 Researchers have vastly different constraints for their budget, environmental conditions in
512 the field, and equipment availability, so “good enough” may be more realistically attainable
513 than the “ideal” radiometric calibration practices described above. If in-flight panel photos
514 are not possible or if only a small panel is available (as is often the case with panels that
515 come with a sensor), photos of the panel can be captured either before or after flight. Many
516 off-the-shelf multispectral sensors only come with one small calibration panel, but having
517 one panel is better than none even though this may limit the data calibration possibilities in
518 the future. Further, popular commercial SfM software like Agisoft Metashape and Pix4D
519 may only accommodate one panel, so correcting UAS imagery with a single panel may be
520 the only practical option. When only a single calibration panel is used, choosing a gray
521 panel (rather than a white or black one) helps to avoid crushing or clipping in under/over
522 exposed images.

523 Regardless of panel cost, color, or material, it is critical to clean, remeasure, recalibrate,
524 and/or replace them over time to ensure the most accurate reflectance calibration possible.
525 This is especially important when field work involves exposing panels to harsh

526 environmental conditions with dirt, dust, sand, sun, and any other types of physical damage
527 or degradation. Illustrating this point, Scholl and Ku (2021) remeasured a calibrated
528 reflectance panel after three years of field work using a handheld Analytical Spectral
529 Devices (ASD, ASD Inc., a Malvern PANalytical Company, Longmont, Colorado) FieldSpec 4
530 spectrometer. Figure 2 depicts the manufacturer-provided panel reflectance spectrum
531 from the time of purchase in 2017 (Micasense) compared to the reflectance spectrum
532 measured three years later with the handheld ASD. The reflectance of the panel has
533 decreased by as much as 10% due to the presence of dirt and dust, especially in the shorter
534 wavelengths. The manufacturer advises against cleaning this make and model of
535 calibration panel as it would force debris further into the pores of the panel material,
536 though newer panels from this manufacturer can be cleaned (see
537 <https://support.micasense.com/hc/en-us/articles/360005163934-Calibrated-Reflectance-Panel-Care-Instructions>). In general, it is key to ensure that the panel reflectance data being
538 used for radiometric calibration accurately represent the panel's actual reflectance, either
539 by using the manufacturer-provided reflectance data for new/clean panels or by using
540 updated reflectance measurements on a panel that can't be restored to its initial conditions.

542 **Georeferencing**

543 It is important to consider how the geographic positions of objects within the UAS survey
544 are used to answer the research question. Those positions can range from being globally
545 accurate with precise correspondence to a location on the Earth (e.g., the tree is located at
546 these coordinates, plus or minus 5 centimeters) to being relatively accurate with the spatial
547 relationships and real-world distances between objects in the scene preserved but perhaps

548 all frame-shifted by some amount compared to reality (e.g., the first tree is 5 meters away
549 from the second tree, but all the trees are shifted 10 meters compared to their true on-the-
550 ground coordinates). In fact, it is possible for the SfM photogrammetry process to
551 reconstruct 3D models and orthomosaics of the area of interest using visual cues in
552 individual images alone without any geolocation data at all, resulting in a relative accuracy
553 between objects in the scene but no ability to make real world measurements (e.g., the
554 distance between the two trees is 5% of the map). In order to infer units from these relative
555 distances (e.g., to get the distance in meters), some measure of scale in the imagery is
556 required. Geolocating the SfM photogrammetry products in real-world space requires
557 external information about the geolocation of each input image, such as from the Global
558 Navigation Satellite System (GNSS). Note that GNSS is the generic term for the network of
559 satellites that offer global coverage of geospatial position, of which the US-owned Global
560 Positioning System (GPS) is a part. Most popular off-the-shelf vehicles and/or optical
561 payloads have a basic GNSS antenna and receiver with an accuracy of <10 m, and the
562 optical data collected will be automatically geotagged in the image metadata. The automatic
563 integration of these metadata in the most popular SfM photogrammetry software means
564 that the second scenario described above- relative spatial accuracy, but with SfM products
565 frame-shifted by some amount similar in magnitude to the GNSS receiver accuracy- is
566 achievable with no extra steps by the user. If greater accuracy is required than what is
567 provided by the built-in GNSS receiver however, then additional steps are required.

568 Ground control points (GCPs), Real-time Kinematic (RTK) corrections, and Post-processed
569 Kinematic (PPK) corrections are three solutions to accurately georeference images
570 collected by the UAS. GCPs are markers laid out on the ground with known geolocations

571 that are visible in the UAS data and are used to tie the UAS imagery to real-world
572 coordinates during the SfM processing step. The GCP approach can only be as precise as the
573 tool used to measure the geolocations of the GCPs in the field. To improve upon the
574 geolocation accuracy already in place by using image metadata geotags from the basic
575 GNSS receiver that is likely onboard the UAS, a high-precision GNSS must be used to mark
576 the geolocations of the GPS. A high-precision GNSS may be prohibitively expensive, but
577 could potentially be borrowed or rented from geodetic services (e.g. nonprofit UNAVCO
578 allows equipment to be borrowed for NSF-funded projects for free). Ideally, GCPs will be
579 placed near edges or randomly throughout the mission area, but the density of GCPs is
580 typically more important, with Santana et al. (2021) finding that 10 GCPs in their 2 ha area
581 of interest were needed for sub-7 cm precision (but 4 GCPs produced 16 cm precision at all
582 flight heights and GCP spatial distributions). Zimmerman et al. (2020) found that it was
583 optimal to place GCPs in the corners of the study site, as well as at low and high elevations
584 within the study site. GCPs must be visible from the sensor, so it's best to place them in
585 bright and open areas. Finding suitable locations in heavily forested areas with closed
586 canopies can be challenging, therefore, it may be beneficial to expand survey areas to
587 include suitable areas for GCPs if none can be found within the area of scientific interest.
588 Examples of effective GCPs are fabric swaths placed in an X, bright-colored bucket lids, or
589 checkered mats (Figure 3). GCPs with more conspicuous, precise points make for more
590 precise geolocating because that specific point can be more easily matched between the
591 field- and UAS-measured data. For instance, trying to identify the exact center of a bright-
592 colored bucket lid from aerial imagery might allow for 10 cm of mismatch with the exact
593 point measured on the ground, the intersection of two, 5-cm wide pieces of cloth might

594 allow for 5 cm of mismatch, and the crisp intersection of the white and black triangles
595 might only allow for 1 cm of mismatch (Figure 3). Because the field measurements of GCP
596 locations can be a slow step, it might be advantageous to install permanent monuments at
597 desirable GCP locations, measure their precise locations once, then reuse those same points
598 during future data collection (e.g., if not the conspicuous marker itself, perhaps a more
599 discrete piece of rebar that can have the actual GCP draped over top of it just prior to new
600 data collection). Pre-existing permanent (or semi-permanent) points may also be used if
601 they can be readily measured on the ground and are visible from the air. For example,
602 NEON TOS plots have permanent markers that have been georeferenced with high
603 precision (approximately 0.3 m) that can be used as GCPs if they are visible to the UAS
604 (Figure 1).

605 RTK and PPK corrections augment the accuracy of a UAS' built-in GNSS receiver by
606 correcting the noise inherent in the instrument using additional equipment and processing
607 steps without the need for laying out GCPs and determining their locations. This can result
608 in massive time savings, particularly when surveying large areas. For instance, Gillan et al.
609 (2021) was able to survey and process data covering over 190 hectares of rangeland in
610 approximately 30 days versus an estimated 141 days using a conventional UAS workflow,
611 with an estimated 47 days saved just from using an RTK system versus GCPs. Even with
612 RTK and PPK corrections, it is still considered good practice to lay out some GCPs at
613 precisely known locations, then quantify geolocation error in the final SfM products by
614 measuring the difference between the field- and UAS-measured GCP locations.

615 **Data management**

616 Image data collected from a UAS can quickly become “big data,” and being intentional about
617 data management will ease friction points at every step in the science workflow, from data
618 collection to manuscript writing (Figure 4). Having a ballpark idea of the total anticipated
619 data storage requirements will help guide data storage hardware purchases such as Secure
620 Digital memory cards (SD cards), external hard drives, internal hard drives, network
621 attached storage (NAS), third-party cloud storage allotments, or university/organization-
622 provided cloud storage allotments. Given the desired flight plan, number of survey areas,
623 and payload (as determined by what meets the science requirements), it should be possible
624 to estimate the amount of data that will be collected per flight, per survey area, and in total
625 for the whole project. It is best practice to adhere as closely as possible to the “3-2-1
626 Backup Rule,” where three copies of the data exist with a local, accessible copy on two
627 different devices (e.g., local computer and an external hard drive) and one copy off-site
628 (e.g., a cloud backup service) (Ruggiero and Heckathorn 2012).

629 UAS optical data are typically collected on SD cards inserted in the sensor, so it is important
630 to have enough empty SD cards prior to flights to accommodate the data being collected in
631 the field. Swapping out the SD card after each flight for an empty one is advisable, so that
632 the only copy of freshly-collected imagery data isn’t lost in the event of a UAS mishap on
633 the next flight. Frequently transferring data from the SD cards to both a laptop hard drive
634 and an external hard drive in the field satisfies the backup rule on having data stored on
635 “two different devices.” Storing those two devices in different locations while in the field
636 (e.g., in two different vehicles, or in the trunk and under the car seat) might prevent some

637 types of data loss (e.g., theft of one of the devices). Once those data are transferred to other
638 devices, it is safe to delete the images on the SD cards in order to reuse them. It's
639 recommended to perform quality assurance (QA) checks on the images while it is still
640 possible to re-collect data. This could mean viewing the images on a laptop on-site, or while
641 still on location near the field study site. Check the data for obvious artifacts such as over or
642 under exposure in images, that the number of images expected were collected, that file
643 sizes appear consistent and reasonable, and that necessary metadata was captured with
644 each image (e.g., the geolocation). Generally a full QA assessment cannot be performed in
645 the field due to time and computation limitations, but the field QA should be sufficient to
646 ensure the images can be processed into desired products. Some NEON sites (e.g., NIWO)
647 have a field house that may be accessed, with permission, for laptop friendly workspaces
648 and/or charging options.

649 Once the data collection is completed, data management can be broken into a quick access
650 phase when data need to be readily available (Figure 4, Short-term storage), and a slower
651 access phase which concerns the longer-term storage of both data and metadata (Figure 4,
652 Long-term storage). During the quick access phase, the data should be as "close" to the
653 workstation doing the SfM processing as possible- ideally on a fast internal hard drive (e.g.,
654 a solid state drive) on the same computer as the SfM software. Having a good long-term
655 storage solution for the imagery (and derived data products) are important for the slower
656 access phase, and having a copy of those data off-site will satisfy the 3-2-1 Backup Rule.
657 Some universities/organizations might already have storage infrastructure capable of
658 accommodating vast data volumes and off-site backups (e.g., Research Computing storage).
659 If university/organization storage infrastructure isn't available, data storage-specific

660 compute hardware (e.g., network attached storage) can be paired with third-party cloud
661 storage (e.g., Cyverse) to meet long-term data management needs. In this case, using slower
662 speed, but lower-cost spinning hard disks instead of solid-state drives is a good option for
663 the local data backup because data volume (i.e., the ability to back up data for many
664 projects) can be prioritized over data access speed in slower access phase. For such high
665 volumes of data, establishing “data levels” that characterize how derived each new
666 processed product is makes them easier to navigate and work with (Wyngaard et al. 2019).
667 Typically, Level 0 represents raw data (the original images from the sensor in the case of
668 optical data) and higher levels are derived from lower levels (e.g., Figure 4 in Koontz et al.
669 2021 shows data levels for optical data collected for a forest ecology project).

670 For public-facing storage, we suggest publishing all data product levels to a long-term data
671 repository with a digital object identifier (DOI) in the open science spirit of broadening
672 access to research (Figure 4, Public-facing). Ideally, this includes the original raw images
673 taken from UAS missions, which may be processed in the future to even higher quality
674 products given the rapid advances in SfM photogrammetry software. This can prove costly
675 with particularly high data volumes, but it may be possible to rely on
676 university/organization cyberinfrastructure resources, or other options that cater
677 specifically to researchers aiming to practice open science principles (e.g., Cyverse, Open
678 Science Framework).

679 **Data processing**

680 One common approach for processing UAS-derived imagery such that it can be integrated
681 with other data sources (e.g., NEON) is SfM photogrammetry, which converts the original

682 images into data products such as a two-dimensional orthomosaic and a three-dimensional
683 point cloud. Many software applications are available for SfM photogrammetry that
684 produce results of similar quality (Forsmoo et al. 2019), and many have steep discounts for
685 research or educational use (e.g., Agisoft Metashape, Pix4DMapper). Some free, open
686 source options are also available (e.g., OpenDroneMap) and are steadily improving. SfM
687 photogrammetry can be CPU, RAM, disk drive, and GPU-intensive, so a workstation that
688 balances these hardware components is ideal. Higher-end gaming desktops are often
689 sufficiently powerful workstations for processing images locally, but cloud-processing
690 options also exist (e.g., university high performance compute resources, add-on capabilities
691 of the specific SfM software purchased, Cyverse– see Swetnam et al. 2018). Even if most of
692 the processing takes place in the cloud, it can still be beneficial to have a relatively powerful
693 local machine in order to readily view and manipulate the resulting data products.

694 SfM workflows require myriad decisions about processing parameters, all of which might
695 affect the quality of the resulting data products. An excellent SfM guide has been published
696 by the US Geological Survey (USGS) for the Agisoft Metashape software (Over et al. 2021),
697 and some researchers have experimented with various SfM processing parameter
698 combinations to empirically determine optimal parameter sets for particular use cases
699 (Tinkham and Swayze 2021, Young et al. 2021) though some trial and error may still be
700 required for new study systems. Some software allow for automating the SfM processing
701 using coding scripts, which then serve as the transparent and reproducible record of the
702 workflow. Other software workflows are based on a point-and-click graphical user
703 interface (GUI), which requires the user to take note of the processing steps. It will
704 eliminate some friction points with resulting SfM products (particularly the three-

705 dimensional point cloud) to work in a coordinate reference system that measures local
706 distances in true units of distance (e.g., distance measured in meters with the Universal
707 Transverse Mercator (UTM) coordinate reference system). In any case, it is important to be
708 consistent with the coordinate reference system for each of your data products (e.g., GNSS
709 positions of GCPs, GNSS locations of UAS camera). When working with optical data, it may
710 be necessary to “spectrally resample” the high spectral resolution NEON AOP in order to
711 match the sensor payload of the UAS, whose spectral resolution is likely coarser and not
712 aligned with that of the NEON instrument (Figure 5). Finally, calculating derived spectral
713 indices such as the Normalized Difference Vegetation Index (NDVI; Rouse et al. (1973))
714 from the original reflectance channels can help with data harmonization across multiple
715 sensors by reducing some of their individual reflectance inaccuracies (Cao et al. 2019).

716 After the SfM workflow is completed, there are many options for further processing the
717 resulting data products (e.g., orthomosaics, point clouds) such that they can be integrated
718 with NEON. Many free, open source software tools exist for working with geospatial data
719 products produced by UAS and NEON including QGIS (<https://qgis.org/en/site/>) for
720 visualization and GUI-based manipulation of raster and vector data types, CloudCompare
721 (<https://www.danielgm.net/cc/>) for visualization and GUI-based manipulation of point
722 clouds, and a suite of packages (<https://cran.r-project.org/web/views/Spatial.html>) for the
723 R programming language (R Core Team 2021). Several packages have also been developed
724 specifically for working with NEON data, including `neonUtilities` (Lunch et al. 2021),
725 `neonhs` (Joseph and Wasser 2021), `geoNEON` (National Ecological Observatory Network
726 2020), and `NeonTreeEvaluation` (Weinstein et al. 2021). A recent review by Atkins et al.
727 (2022) describes the ecosystem of R packages available for working with forestry data,

728 many of which are relevant for the types of geospatial data produced by UAS and NEON.
729 More generally, working with these kinds of high-resolution geospatial data, which are
730 often classically “big,” can benefit from following the few simple rules recently outlined by
731 Joseph et al. (2021).

732 Case study

733 Science requirements

734 Forest inventories describe the geolocation and physical attributes of individual trees, and
735 provide critical information for management decision-making and advancing ecological
736 theory (Young et al. 2021). Remote sensing approaches to creating forest inventories can
737 cover more area than field-based methods at a lower cost per area, and recent approaches
738 still allow for characterization of individual trees (Weinstein et al. 2019). The NEON TOS
739 collects field-based forest inventory data (the “Woody Plant Vegetation Structure” data
740 product; DP1.10098.001) and remote sensing data in their AOP that have been used to
741 generate forest inventory data (Weinstein et al. 2020). The field-based data are restricted
742 to 20 x 20m field plots, while the AOP data cover dozens of square kilometers but at
743 moderately coarse resolution (10 cm for RGB imagery, 1 m for imaging spectrometer data,
744 1 m for LiDAR data). UAS have the capacity to fill in missing scales of observation for
745 creating forest inventories by capturing a broader spatial extent than field-based NEON
746 data, but at a finer spatial resolution than NEON AOP data. With this as a motivation, here
747 we present a case study where we collect and process UAS data coincident with a NEON
748 TOS plot to create a forest inventory. We then benchmark that forest inventory against the

749 NEON TOS field data, and describe how to extract individual tree-scale spectral information
750 that is comparable to that collected by the NEON AOP. We use the previous section's "core
751 principles" as a framework for describing our workflow, and provide all data and code to
752 further aid our mental model building.

753 **Vehicle**

754 Our vehicle was a DJI Matrice 100 rotocopter with four propellers and a proven track
755 record of safe, predictable flights. The vertical takeoffs and landings of the rotocopter style
756 drone allowed us to operate the vehicle from a clearing as small as the width of the dirt
757 access road to the site. We used a piece of plywood laid on the ground as a flat, stable
758 takeoff platform that would also help to minimize the amount of dust kicked up by the
759 rotor wash during takeoff and landing. The Matrice 100 has a relatively high lift capacity
760 that allows for a payload to be integrated, and is heavier than many consumer rotocopters
761 which makes it both more stable in windy conditions and more challenging to transport
762 beyond a road.

763 **Payload**

764 We captured imagery using two co-mounted sensors: a gimbal-stabilized DJI Zenmuse X3
765 RGB camera, and a MicaSense RedEdge 3 sensor, which is sensitive to electromagnetic
766 radiation in five distinct spectral channels across the visible and near infrared wavelengths.
767 The DJI Zenmuse X3 camera has a focal length of 3.6 mm, a sensor width of 6.17 mm, and a
768 sensor height of 4.55 mm. The MicaSense RedEdge 3 sensor has a focal length of 5.5 mm, a
769 sensor width of 4.8 mm, and a sensor height of 3.6 mm. We used a fixed mount and a

770 prebuilt integration kit for the MicaSense RedEdge 3 made by the sensor manufacturer to
771 integrate with our vehicle. This particular mount is angled such that the sensor faces
772 exactly downward when the aircraft is tilted forward in flight, and the integration kit
773 allows the sensor to share power with the vehicle batteries. The RedEdge 3 sensor image
774 capture mechanism is independent from the flight planning app or the vehicle's flight
775 computer, though deeper integration with specific vehicles is possible with newer versions
776 of the sensor. Prior to flight, we connected to the RedEdge 3 sensor with a laptop via its
777 built-in WiFi to verify that the sensor's onboard GNSS receiver was functioning properly
778 and to initiate image capture. We set the RedEdge 3 sensor to capture images at a rate of 1
779 image per second. We set the DJI Zenmuse X3 camera to capture images at a rate of 0.5
780 images per second. Using the quantum efficiency and filter bandpass sensitivity of an
781 average RedEdge 3 sensor provided by MicaSense, we estimated the relative spectral
782 response of the instrument which characterizes how the sensor captures light across the
783 electromagnetic spectrum (Figure 5). We provide the relative spectral response data in a
784 format that makes it interoperable with the hsdar package (Lehnert et al. 2019).

785 **Environment**

786 Our data collection took place on a single day under mostly sunny, light wind conditions on
787 October 9th, 2019 starting at 2pm mountain daylight time. We ideally would have flown
788 closer to solar noon to minimize shadows in the imagery, particularly this late in the year.

789 **Flight planning**

790 We used Map Pilot for DJI, an Apple iPad iOS app, for planning the flight. Map Pilot is a
791 reliable, full-featured flight planning application that allows us to set flight parameters such
792 as forward overlap, side overlap, and sensor angle. We flew at an altitude of 100 m, and set
793 the forward overlap to 95% and side overlap to 80% (based on the built-in DJI RGB camera,
794 the Zenmuse X3). We used a zero-degree sensor angle (i.e., downward/nadir facing), and
795 added a perpendicular set of aerial transects to create a crosshatch flight pattern (Figure
796 1). We opted to plan flights with particularly high overlap so that we had the option to
797 remove photos at different intervals prior to SfM processing in order to test how various
798 photo densities affected our UAS-derived forest inventory benchmark against NEON TOS
799 field data. The Map Pilot software determines flight parameters such as flight speed and
800 distance between aerial transects based on the user-desired front/side overlap, which are
801 themselves based on the built-in DJI camera. We calculated these flight parameters as
802 follows:

$$\begin{aligned}x_{ground,x3} &= a_{vehicle} \frac{x_{sensor,x3}}{f_{sensor,x3}} \\y_{ground,x3} &= a_{vehicle} \frac{y_{sensor,x3}}{f_{sensor,x3}} \\t_{vehicle} &= (1 - o_{side,x3})(x_{ground,x3}) \\s_{vehicle} &= (1 - o_{front,x3})(y_{ground,x3})(s_{shutter,x3})\end{aligned}$$

803 Where $x_{ground,x3}$ is the horizontal dimension of the Zenmuse X3 sensor's ground footprint
804 in m, $y_{ground,x3}$ is the vertical dimension of the Zenmuse X3 sensor's ground footprint in m,
805 $a_{vehicle}$ is the vehicle's altitude during image capture in m, $x_{sensor,x3}$ is the width of the
806 Zenmuse X3 sensor in mm, $y_{sensor,x3}$ is the height of the Zenmuse X3 sensor in mm,
807 $f_{sensor,x3}$ is the focal length of the Zenmuse X3 sensor in mm, $s_{shutter,x3}$ is the shutter speed in s,

808 $f_{sensor,x3}$ is the focal length of the Zenmuse X3 sensor, $t_{vehicle}$ is the transect spacing
809 between aerial transects of the vehicle in m, $o_{side,x3}$ is the planned side overlap of the
810 Zenmuse X3 imagery as a fraction, $o_{front,x3}$ is the planned front overlap of the Zenmuse X3
811 imagery as a fraction, $s_{vehicle}$ is the speed of the vehicle in m/s, and $s_{shutter,x3}$ is the
812 planned shutter speed of the Zenmuse X3 sensor.

813 Because the MicaSense RedEdge 3 has a different optical geometry than the Zenmuse X3
814 camera, we can use the flight parameters calculated above to determine the actual overlap
815 of the imagery from the MicaSense RedEdge 3:

$$\begin{aligned}x_{ground,RE3} &= a_{vehicle} \frac{x_{sensor,RE3}}{f_{sensor,RE3}} \\y_{ground,RE3} &= a_{vehicle} \frac{y_{sensor,RE3}}{f_{sensor,RE3}} \\o_{side,RE3} &= 1 - \frac{t_{vehicle}}{x_{ground,RE3}} \\o_{front,RE3} &= 1 - \frac{s_{vehicle}}{(s_{shutter,RE3})(y_{ground,RE3})}\end{aligned}$$

816
817 Where $x_{ground,RE3}$ is the horizontal dimension of the MicaSense RedEdge 3 sensor's ground
818 footprint in mm, $y_{ground,RE3}$ is the vertical dimension of the RedEdge 3 sensor's ground
819 footprint in m, $x_{sensor,RE3}$ is the width of the RedEdge 3 sensor in mm, $y_{sensor,RE3}$ is the
820 height of the RedEdge 3 sensor in mm, $f_{sensor,RE3}$ is the focal length of the RedEdge 3
821 sensor, $o_{side,RE3}$ is the calculated side overlap of the RedEdge 3 imagery as a fraction,
822 $o_{front,RE3}$ is the calculated front overlap of the RedEdge 3 imagery as a fraction, and
823 $s_{shutter,RE3}$ is the planned shutter speed of the RedEdge 3 sensor.

824 Using the front and side overlap, we can estimate the approximate number of images
825 captured of each point within the survey area for the Zenmuse X3 sensor, p_{x3} , and the
826 MicaSense RedEdge 3 sensor, p_{RE3} , as:

$$p_{x3} = \frac{1}{(1 - o_{side,x3})(1 - o_{front,x3})}$$
$$p_{RE3} = \frac{1}{(1 - o_{side,RE3})(1 - o_{front,RE3})}$$

827
828 The code for these calculations can be found at https://github.com/mikoontz/neon-drone-workflow/blob/master/workflow/02_preprocess-drone-data/03_drone_L0_image-overlap-calculator.R.
829
830

831 Our aerial transects were 17.14 m apart, our vehicle flew at 3.16 m/s, the side overlap of
832 the RedEdge 3 imagery was 80.4%, and the front overlap of the RedEdge 3 imagery was
833 95.2%. The estimated number of photos per point in the survey area was 200 for the
834 Zenmuse X3 camera, and 105.5 for the MicaSense RedEdge 3 sensor. The crosshatch flight
835 plan effectively doubles the expected number of photos per point to 400 for the X3 camera
836 and 211.0 for the RedEdge 3 (Figure 1).

837 **Regulations**

838 We obtained permission to access the NIWO NEON site from the site host, the University of
839 Colorado Boulder Mountain Research Station, as well as NEON itself. We flew under the
840 FAA Part 107 rules for commercial drone operations with a current remote pilot certificate,
841 and ensured that the airspace was free for operating the UAS.

842 **Radiometric calibration**

843 The MicaSense RedEdge 3 multispectral camera comes with a small, gray calibrated
844 reflectance panel that reflects approximately 60% of light across the entire spectral extent
845 captured by the sensor. We held the UAS over the panel and captured an image of the
846 calibration panel prior to flight ensuring our shadow didn't cover the panel. The RedEdge 3
847 also integrates a DLS, which faces upwards and measures illumination at the same time as
848 the downward-facing image capture. We included the calibration panel photos in the SfM
849 processing workflow and also enabled the image-to-image corrections from the DLS. When
850 loading the calibration panel photos into the SfM software, we set the "known reflectance"
851 of the panel in each of the five spectral channels to be those that we measured for this
852 particular panel (Figure 2), rather than those provided by the manufacturer.

853 **Georeferencing**

854 We laid out orange cloth X's over the 9 permanent markers within the NIWO_017 field site
855 (red points in Figure 1). Five of these points were visible from the air. These ground control
856 points were located within the center of the flight area, without any geolocation
857 representation at the edges which wasn't ideal (Zimmerman et al. 2020, Santana et al.
858 2021).

859 **Data management**

860 For data collection, we recorded each flight's imagery on a separate 32 GB SD card rated at
861 >90 MB/s write speed. For multi-day trips or if SD cards need to be reused, we transfer
862 imagery from the SD cards to at least one portable solid state hard drive (Samsung T

863 series). Upon returning from the field, we transferred images from the SD cards (or
864 portable solid state hard drive, as the case may be) to two locations: 1) the solid state hard
865 drive on a local desktop gaming computer for short term storage and processing, and 2) a
866 Network Attached Storage (NAS) with 6 spinning disk hard drives in a RAID array for long-
867 term storage. Both the short-term storage (local desktop) and long-term storage (NAS)
868 solutions are backed up to the cloud using a 3rd party backup client (Backblaze) at a cost of
869 ~\$5.00 USD per terabyte per month. We use the same data levels as Koontz et al. (2021),
870 except we didn't process our data to Level 4. To allow for future data collection to integrate
871 easily into this project, we compartmentalized each data product to a folder for the specific
872 flight date (2019-10-09), which was housed in a folder for the specific flight location
873 (NIWO_017). We used the Open Science Framework for public-facing storage
874 (<https://doi.org/10.17605/OSF.IO/ENBWU>).

875 **Data processing**

876 We used a local desktop computer (Alienware Aurora R7 with an Intel i7-8700k 3.70 GHz
877 hexacore processor and 64 GB of RAM) for data processing. We followed the USGS
878 workflow to process our raw MicaSense RedEdge 3 imagery into a digital surface model, an
879 orthomosaic and a dense point cloud using Agisoft Metashape version 1.6.1 (Over et al.
880 2021). We noted each step in the SfM process, as well as the parameter choices we made, in
881 a .txt file (https://github.com/mikoontz/neon-drone-workflow/blob/master/workflow/03_structure-from-motion-of-drone-data/01_drone_agisoft-metashape-processing-steps.txt). We created a script to allow
884 readers to download cropped versions of these SfM products that are relatively small in

885 size in order to follow along with our post-SfM processing steps
886 (https://github.com/mikoontz/neon-drone-workflow/blob/master/workflow/04_get-
887 [processed-example-drone-data/01_get-example-cropped-L1-and-L2-data.R](#)). We used R for
888 all post-SfM steps, particularly the `sf` package for working with vector data (Pebesma
889 2018) and the `terra` package (Hijmans 2021a) for working with raster data. The `terra`
890 package is intended to be a replacement for the `raster` package (Hijmans 2021b), but some
891 other R packages haven't yet migrated their codebase to use `terra`. In these cases, we
892 coerce `terra` objects to be `raster` objects in order to preserve the interoperability of the
893 various packages.

894 We classified the dense point cloud into "ground" and "non-ground" points using a cloth
895 simulation filter algorithm (Zhang et al. 2016) implemented in the `lidR` (Roussel and Auty
896 2021) package. Using the ground points, we interpolated a digital terrain model (DTM)
897 representing the height of the ground (without the vegetation). We subtracted this DTM
898 from the SfM-derived digital surface model to create a canopy height model (CHM)
899 representing the height of the vegetation in the survey area.

900 To integrate our UAS data with NEON TOS field data, we used the CHM to detect and
901 segment individual tree crowns. We used a variable window filter to detect individual
902 trees, which searches for all of the maximum heights in a CHM within a circle of variable
903 radius defined by the height of each pixel in that CHM in turn (Popescu and Wynne 2004).
904 That is, pixels in the CHM representing taller vegetation will have a broader search radius
905 within which the location of the maximum height is determined. We used the `ForestTools`
906 package to implement this algorithm and used the optimal tree detection parameter set

907 determined by Young et al. (2021) for a structurally complex mixed-conifer forest, with a
908 variable search window defined using the following function:

909

$$r = 0.04x$$

910 Where r is the radius of the variable search window, and x is the canopy height of the focal
911 pixel.

912 Using the detected trees, we implemented a marker controlled watershed segmentation
913 algorithm using the `ForestTools` package to segment individual tree crowns (Plowright
914 and Roussel 2021). For each tree crown, we created a new geometry representing its
915 bounding box (i.e., the smallest rectangle that fully contains the irregularly-shaped crown
916 polygon) in order to compare UAS-derived crown segments to those derived using deep
917 learning approaches (Weinstein et al. 2019). We benchmarked our tree detection using the
918 `NeonTreeEvaluation` package (Weinstein et al. 2021) to compare our tree detections with
919 the NEON TOS field-collected tree locations and with previously-annotated crown
920 bounding boxes derived from NEON AOP imagery (Weinstein et al. 2021). The stem
921 locations of the trees in the NEON TOS sites can be determined using a combination of the
922 `neonUtilities` package (Lunch et al. 2021) to download the `geoNEON` package (National
923 Ecological Observatory Network 2020), but they are also directly available in the
924 `NeonTreeEvaluation` package. Within the NIWO_017 plot, we detected 60% of the field-
925 measured stems (i.e., a recall score of 0.6). Comparison with the annotated crowns using
926 the `compute_precision_recall()` function in the `NeonTreeEvaluation` package also
927 provides precision scores (a measure of the false positive tree detection rate) which can be

928 combined with the recall scores (a measure of the true positive tree detection rate) in an
929 integrated measure of predictive ability called the F-score:

$$\begin{aligned} p &= \frac{T_{reference} \cap T_{UAS}}{T_{UAS}} \\ r &= \frac{T_{reference} \cap T_{UAS}}{T_{reference}} \\ F &= \frac{2 * p * r}{p + r} \end{aligned}$$

930
931 Where p is the precision, r is the recall, F is the F-score, $T_{reference}$ is the number of
932 reference trees (e.g., those identified in a field survey), T_{UAS} is the number of trees detected
933 by the UAS, and $T_{reference} \cap T_{UAS}$ is the number of reference trees that were correctly
934 detected by the drone (i.e., the true positive detections).

935 For our comparison, we set the threshold argument of the `compute_precision_recall()`
936 function to 0.1 such that a predicted tree was considered correctly predicted if the
937 intersection of its bounding box with an annotated crown's bounding box divided by the
938 area of the union of those bounding boxes is greater than 0.1. Our UAS-derived map of
939 detected trees had a recall of 0.788 and a precision of 0.276, resulting in an F-score of
940 0.409. For comparison, the DeepForest algorithm's predictions for the locations of trees at
941 NIWO_017 (Weinstein et al. 2021) had a recall of 0.861, a precision of 0.798, and an F-score
942 of 0.828. The poorer performance of the UAS-derived tree detection approach suggests that
943 a different combination of flight parameters, SfM photogrammetry parameters, or tree
944 detection algorithm/parameters might be better suited to the subalpine forest at NIWO
945 (Young et al. 2021).

946 To integrate our UAS data with NEON AOP reflectance data, we calculated NDVI from each
947 sensor. We used the `neonUtilities` package to download the NEON AOP imaging
948 spectrometer data (data product DP3.30006.001) that covers the NIWO_017 site from
949 2019, using the easting and northing of the centroid of the NIWO_017 plot and a 20 m
950 buffer as arguments to the `byTileAOP()` function (Lunch et al. 2021). We used the `neonhs`
951 (Joseph and Wasser 2021) package to convert the raw NEON AOP data product into a
952 raster object more readily manipulatable in R. Because the imaging spectrometer spectral
953 response overlaps with, but doesn't perfectly align with the spectral response of the
954 MicaSense RedEdge 3 sensor, we spectrally resampled the NEON AOP data to match the
955 spectral resolution of the MicaSense RedEdge 3 sensor using the `hsdar` package (Lehnert et
956 al. 2019) and the relative spectral response that we derived (Figure 5). We used the UAS-
957 derived orthomosaic and the spectrally-resampled NEON AOP orthomosaic to calculate
958 NDVI. Figure 6 shows the comparison between NDVI as captured by the NEON AOP flight in
959 August with our UAS-derived NDVI from our flight in October. We used the `exactextractr`
960 package to extract the mean and standard deviation of NDVI derived from the UAS as well
961 as the spectrally resampled NEON AOP for each segmented tree crown (Daniel Baston
962 2021). Figure 7 shows the comparison of NDVI derived from the NEON AOP and the UAS at
963 an individual tree scale.

964 **Discussion**

965 Macroecology will benefit from a “macroscope” to enable the study of broad-extent
966 phenomena across multiple scales of biological, geophysical, and social processes (Lawton

967 1996, Beck et al. 2012, Dornelas et al. 2019). The ideal macroscope comprises a nested
968 array of tools that provide full coverage of spatial and temporal observational domains. In
969 their complementarity, the value of multiple observational tools in concert is more than the
970 sum of the parts (Dornelas et al. 2019). Pairing UAS with NEON partially completes the
971 constellation of Earth observing tools that contribute to the macroscope, and combines the
972 flexibility of UAS with the high quality and consistency of NEON. In this work, we aid the
973 adoption of these tools among macroecologists by providing a mental model– a contextual
974 framework– and some practical considerations for their integration.

975 **Challenges**

976 Challenges remain for integrating UAS with NEON, but they are surmountable. Some of
977 these challenges are fundamentally associated with “big,” cross-scale data. Integrating data
978 across scales brings a host of potential pitfalls that could pollute inference if care isn’t taken
979 to avoid them (Zipkin et al. 2021). Big data in ecology are relatively new (Farley et al.
980 2018), and approaches to UAS-derived big data are fairly ad hoc across researchers
981 (Wyngaard et al. 2019). Maintaining supportive communities of practice, such as the High
982 Latitude Drone Ecology Network (<https://arcticdrones.org/>), can help overcome some of
983 these idiosyncratic approaches. In the same vein, NEON provides an aspirational target for
984 UAS educational resources, which are critical to ensuring that would-be NEON/UAS users
985 have the environmental data science skills necessary to turn their data into inference
986 (Hampton et al. 2017).

987 The proliferation of reasonably low-cost, off-the-shelf, drone-ready sensors (many
988 designed for precision agriculture use) creates a need for validation of whether those

989 instruments produce “science grade” data (which itself is a relative term, depending on
990 what the specific science requirements are for a given project). This validation may be
991 achieved via direct comparison of the low-cost sensors with “state of the science”
992 instruments using coincident flights (e.g., Fawcett et al. 2020). Clear documentation of data
993 provenance including sensor characteristics, data acquisition methods (e.g., flight pattern),
994 and data acquisition conditions (e.g., time of day, cloud cover) will enable more rigorous
995 data integration across instruments. Thus, integrating UAS operations with NEON can help
996 anchor the community to the common currency of NEON data types, organization, and
997 collection protocols which will enhance the interoperability of UAS data.

998 Cyberinfrastructure for managing and processing UAS data is not yet built in a way that
999 encourages consistency between projects or researchers. In this way, NEON again provides
1000 an aspirational example for how purpose-built cyberinfrastructure can facilitate
1001 macroecology. In fact, the foundational resources for building a valuable architecture for
1002 UAS data may already be represented in other NSF-sponsored projects (e.g., Cyverse,
1003 OpenTopography, Open Science Framework). UAS-enabled research would benefit greatly
1004 from data storage solutions and streamlined analysis pipelines that are intentionally built
1005 to support a wide variety of users and use cases.

1006 Critically, “accessibility” and “democratization” of macroecology encompass a broad,
1007 multifaceted notion of availability for and usability by anyone, and obstacles to accessibility
1008 extend beyond those we sought to remedy here. That is, our work to increase access to the
1009 elusive broad-extent/fine-grain observational domain with a mental model and an open
1010 workflow is an important, but incomplete effort towards accessible macroecology.

1011 Illustrating this point, the reduced cost of Landsat images brought more researchers into
1012 the user base from lower-resourced institutions and underrepresented parts of the world
1013 to do more topically diverse science (Nagaraj et al. 2020), but some barriers to access still
1014 exist (Miller et al. 2016). For instance, three-quarters of users are men, and 65% of users
1015 are academic researchers (Miller et al. 2016). The Landsat archive was undeniably made
1016 more accessible, to the collective benefit of science and society (Miller 2016, Nagaraj et al.
1017 2020), but even broader access (and therefore greater value; Miller 2016) is possible.
1018 Greater accessibility of UAS and NEON as tools for macroecology will similarly require their
1019 user communities to be self-reflective and proactive about identifying and eliminating
1020 barriers to entry (Nagy et al. 2021).

1021 **Future directions**

1022 We conclude with a set of research themes that are well-suited for UAS/NEON integration
1023 with example ecology applications, which we hope provides a vision to be built upon:

- 1024 1. Filling in spatial scales missed by NEON data collection (e.g., collecting data on a
1025 similar vegetation type of a NEON site but outside of NEON's direct footprint,
1026 capturing data at spatial resolutions finer than 10 cm in order to measure post-
1027 disturbance vegetation recovery)
- 1028 2. Filling in temporal scales missed by NEON data collection (e.g., capturing data in a
1029 year when a NEON site is skipped by the AOP, capturing data at a site multiple times
1030 per year to understand how snowpack changes through the year, tracking individual
1031 plant phenology through time and linking to phenocam data; understanding
1032 temporal trends in biodiversity)

- 1033 3. Opportunistic data collection (e.g., capturing data immediately after a disturbance
1034 event to measure its severity)
- 1035 4. Connecting NEON data to other Earth observing systems using UAS data as a bridge
1036 (e.g., spectrally unmixing Landsat pixels to determine relative species compositions
1037 by matching UAS spectral measurements to NEON TOS field measurements;
1038 coordinating NEON data collection with UAS and other data collection to expand the
1039 utility of NEON products (e.g., Chadwick et al. 2020, Wang et al. 2020))
- 1040 5. Supplementing NEON data using sensors that aren't part of the NEON suite of
1041 sensors (e.g., thermal data to compare thermal regulation of different plant species,
1042 measuring water stress in different trees across gradients of topoclimate)
- 1043 6. Validating lower cost, off-the-shelf payloads against the state-of-the-science NEON
1044 data collection (e.g., determining how well a multispectral imager designed for
1045 agriculture captures surface reflectance, determining how well an algorithm detects
1046 the trees in a NEON vegetation structure plot)
- 1047 7. Replacing high-cost NEON AOP flights with lower-cost alternatives (e.g., if the
1048 drone-derived data are "good enough" compared to the AOP, can we reduce the
1049 operational costs of the AOP)
- 1050 8. Using NEON data as a common currency for validating new methods (e.g., the case
1051 study we showed here, comparing a deep learning/orthomosaic based approach
1052 and a variable window filter/canopy height model approach to detecting individual
1053 trees measured by the NEON TOS)

1054 UAS integration can help ecologists harness the NEON data revolution with its
1055 complementary approach to measuring the understudied broad extent/fine-grain
1056 observational domain. NEON's long-term, consistent, high-quality, continental extent
1057 measurements enable data-driven discovery that is enhanced with new opportunities to
1058 explore cross-scale questions when paired with the relatively affordable, flexible
1059 measurements of UAS. We hope that by providing a mental model for data collection and
1060 integration, we remove some of the friction points associated with these tools and make
1061 them more accessible. Further democratizing macroecology will require community
1062 support for an open science ethos, which might include: low-cost cyberinfrastructure, open
1063 observatories, data networks, well-documented workflows, open education resources that
1064 increase data skills, and more inclusive practices that create opportunities for researchers
1065 across a diversity of career stages and institutions to participate in and contribute to 'big
1066 data' macroecology. We envision NEON as an anchor for UAS-enabled ecology, with future
1067 research efforts that embrace the spirit of democratization and strive to broaden
1068 participation in this emerging discipline.

1069 Acknowledgements

1070 Funding for the 2019 NEON Science Summit was provided by NSF Award #1906144.
1071 Additional funding was provided by Earth Lab through the University of Colorado,
1072 Boulder's Grand Challenge Initiative, the Cooperative Institute for Research in
1073 Environmental Sciences, and the U.S. Geological Survey North Central Climate Adaptation
1074 Science Center. M. E. Cattau was supported in part by the National Aeronautics and Space

1075 Administration (NASA) New Investigator Program (NIP) (grant 80NSSC18K0750). J. K.
1076 Balch was supported in part by the National Science Foundation's CAREER (grant
1077 #1846384) and Macrosystems (grant #2017889) programs. The National Ecological
1078 Observatory Network is a program sponsored by the National Science Foundation and
1079 operated under cooperative agreement by Battelle. This material is based in part upon
1080 work supported by the National Science Foundation through the NEON Program. We thank
1081 Chelsea Nagy, Jeff Sloan, Natalie Latysh, Harland Goldstein, and two anonymous reviewers
1082 for their feedback, which greatly improved the manuscript. Any use of trade, firm, or
1083 product names is for descriptive purposes only and does not imply endorsement by the U.S.
1084 Government.

1085 **References**

- 1086 Adão, T., J. Hruška, L. Pádua, J. Bessa, E. Peres, R. Morais, and J. Sousa. 2017. Hyperspectral
1087 imaging: A review on UAV-based sensors, data processing and applications for agriculture
1088 and forestry. *Remote Sensing* 9:1110.
- 1089 Alvarez, M. 2020. Forest Inventory and Analysis, Fiscal Year 2019 Business Report. Page 84.
1090 USDA Forest Service.
- 1091 Anderson, K., and K. J. Gaston. 2013. Lightweight unmanned aerial vehicles will
1092 revolutionize spatial ecology. *Frontiers in Ecology and the Environment* 11:138–146.
- 1093 Asner, G. P., D. E. Knapp, J. Boardman, R. O. Green, T. Kennedy-Bowdoin, M. Eastwood, R. E.
1094 Martin, C. Anderson, and C. B. Field. 2012. Carnegie Airborne Observatory-2: Increasing

- 1095 science data dimensionality via high-fidelity multi-sensor fusion. *Remote Sensing of*
1096 *Environment* 124:454–465.
- 1097 Asner, G. P., D. E. Knapp, T. Kennedy-Bowdoin, M. O. Jones, R. E. Martin, J. Boardman, and C.
1098 B. Field. 2007. Carnegie Airborne Observatory: In-flight fusion of hyperspectral imaging
1099 and waveform light detection and ranging (wLiDAR) for three-dimensional studies of
1100 ecosystems. *Journal of Applied Remote Sensing* 1:013536.
- 1101 Asner, G. P., J. Mascaro, C. Anderson, D. E. Knapp, R. E. Martin, T. Kennedy-Bowdoin, M. van
1102 Breugel, S. Davies, J. S. Hall, H. C. Muller-Landau, C. Potvin, W. Sousa, J. Wright, and E.
1103 Bermingham. 2013. High-fidelity national carbon mapping for resource management and
1104 REDD+. *Carbon Balance and Management* 8:7.
- 1105 Assmann, J. J., J. T. Kerby, A. M. Cunliffe, and I. H. Myers-Smith. 2019. Vegetation monitoring
1106 using multispectral sensors best practices and lessons learned from high latitudes. *Journal*
1107 *of Unmanned Vehicle Systems* 7:54–75.
- 1108 Atkins, J. W., A. E. L. Stovall, and C. Alberto Silva. 2022. Open-Source tools in R for forestry
1109 and forest ecology. *Forest Ecology and Management* 503:119813.
- 1110 Balch, J. K., R. C. Nagy, and B. S. Halpern. 2020. NEON is seeding the next revolution in
1111 ecology. *Frontiers in Ecology and the Environment* 18:3–3.
- 1112 Beck, J., L. Ballesteros-Mejia, C. M. Buchmann, J. Dengler, S. A. Fritz, B. Gruber, C. Hof, F.
1113 Jansen, S. Knapp, H. Kreft, A.-K. Schneider, M. Winter, and C. F. Dormann. 2012. What's on
1114 the horizon for macroecology? *Ecography* 35:673–683.

- 1115 Cao, S., B. Danielson, S. Clare, S. Koenig, C. Campos-Vargas, and A. Sanchez-Azofeifa. 2019.
- 1116 Radiometric calibration assessments for UAS-borne multispectral cameras: Laboratory and
- 1117 field protocols. *ISPRS Journal of Photogrammetry and Remote Sensing* 149:132–145.
- 1118 Chadwick, K. D., P. G. Brodrick, K. Grant, T. Goulden, A. Henderson, N. Falco, H. Wainwright,
- 1119 K. H. Williams, M. Bill, I. Breckheimer, E. L. Brodie, H. Steltzer, C. F. R. Williams, B. Blonder, J.
- 1120 Chen, B. Dafflon, J. Damerow, M. Hancher, A. Khurram, J. Lamb, C. R. Lawrence, M.
- 1121 McCormick, J. Musinsky, S. Pierce, A. Polussa, M. Hastings Porro, A. Scott, H. W. Singh, P. O.
- 1122 Sorensen, C. Varadharajan, B. Whitney, and K. Maher. 2020. Integrating airborne remote
- 1123 sensing and field campaigns for ecology and Earth system science. *Methods in Ecology and*
- 1124 *Evolution* 11:1492–1508.
- 1125 Cunliffe, A. M., R. E. Brazier, and K. Anderson. 2016. Ultra-fine grain landscape-scale
- 1126 quantification of dryland vegetation structure with drone-acquired structure-from-motion
- 1127 photogrammetry. *Remote Sensing of Environment* 183:129–143.
- 1128 Dandois, J. P., and E. C. Ellis. 2013. High spatial resolution three-dimensional mapping of
- 1129 vegetation spectral dynamics using computer vision. *Remote Sensing of Environment*
- 1130 136:259–276.
- 1131 Dandois, J., M. Olano, and E. Ellis. 2015. Optimal Altitude, Overlap, and Weather Conditions
- 1132 for Computer Vision UAV Estimates of Forest Structure. *Remote Sensing* 7:13895–13920.
- 1133 Daniel Baston. 2021. Exactextractr: Fast extraction from raster datasets using polygons.
- 1134 manual.

- 1135 Degani, A., and E. L. Wiener. 1993. Cockpit checklists: Concepts, design, and use. *Human*
1136 *Factors* 35:345–359.
- 1137 Díaz, G. M., D. Mohr-Bell, M. Garrett, L. Muñoz, and J. D. Lencinas. 2020. Customizing
1138 unmanned aircraft systems to reduce forest inventory costs: Can oblique images
1139 substantially improve the 3D reconstruction of the canopy? *International Journal of*
1140 *Remote Sensing* 41:3480–3510.
- 1141 Dornelas, M., E. M. P. Madin, M. Bunce, J. D. DiBattista, M. Johnson, J. S. Madin, A. E.
1142 Magurran, B. J. McGill, N. Pettorelli, O. Pizarro, S. B. Williams, M. Winter, and A. E. Bates.
1143 2019. Towards a macroscope: Leveraging technology to transform the breadth, scale and
1144 resolution of macroecological data. *Global Ecology and Biogeography* 28:1937–1948.
- 1145 Ernest, S. K. M. 2018. Scales of data. *Nature Ecology & Evolution* 2:769–770.
- 1146 Estes, L., P. R. Elsen, T. Treuer, L. Ahmed, K. Caylor, J. Chang, J. J. Choi, and E. C. Ellis. 2018.
1147 The spatial and temporal domains of modern ecology. *Nature Ecology & Evolution* 2:819–
1148 826.
- 1149 Farley, S. S., A. Dawson, S. J. Goring, and J. W. Williams. 2018. Situating Ecology as a Big-Data
1150 Science: Current Advances, Challenges, and Solutions. *BioScience* 68:563–576.
- 1151 Fawcett, D., C. Panigada, G. Tagliabue, M. Boschetti, M. Celesti, A. Evdokimov, K. Biriukova,
1152 R. Colombo, F. Miglietta, U. Rascher, and K. Anderson. 2020. Multi-scale evaluation of
1153 drone-based multispectral surface reflectance and vegetation indices in operational
1154 conditions. *Remote Sensing* 12:514.

- 1155 Forsmoo, J., K. Anderson, C. J. A. Macleod, M. E. Wilkinson, L. DeBell, and R. E. Brazier. 2019.
- 1156 Structure from motion photogrammetry in ecology: Does the choice of software matter?
- 1157 *Ecology and Evolution* 9:12964–12979.
- 1158 Frey, J., K. Kovach, S. Stemmler, and B. Koch. 2018. UAV photogrammetry of forests as a
1159 vulnerable process. A sensitivity analysis for a structure from motion RGB-image pipeline.
- 1160 *Remote Sensing* 10:912.
- 1161 Gillan, J., G. E. Ponce-Campos, T. L. Swetnam, A. Gorlier, P. Heilman, and M. P. McClaran.
1162 2021. Innovations to expand drone data collection and analysis for rangeland monitoring.
1163 bioRxiv:2021.02.05.430004.
- 1164 Gillespie, A. J. R. 1999. Rationale for a National Annual Forest Inventory Program. *Journal of
1165 Forestry* 97:16–20.
- 1166 Goodbody, T. R. H., N. C. Coops, P. L. Marshall, P. Tompalski, and P. Crawford. 2017.
1167 Unmanned aerial systems for precision forest inventory purposes: A review and case study.
1168 *The Forestry Chronicle* 93:71–81.
- 1169 Gorelick, N., M. Hancher, M. Dixon, S. Ilyushchenko, D. Thau, and R. Moore. 2017. Google
1170 Earth Engine: Planetary-scale geospatial analysis for everyone. *Remote Sensing of
1171 Environment* 202:18–27.
- 1172 Guston, D. H. 2004. Forget politicizing science. Let's democratize science! *Issues in Science
1173 and Technology* 21:25–28.
- 1174 Hampton, S. E., M. B. Jones, L. A. Wasser, M. P. Schildhauer, S. R. Supp, J. Brun, R. R.
1175 Hernandez, C. Boettiger, S. L. Collins, L. J. Gross, D. S. Fernández, A. Budden, E. P. White, T. K.

- 1176 Teal, S. G. Labou, and J. E. Aukema. 2017. Skills and knowledge for data-intensive
1177 environmental research. *Bioscience* 67:546–557.
- 1178 Hampton, S. E., C. A. Strasser, J. J. Tewksbury, W. K. Gram, A. E. Budden, A. L. Batcheller, C. S.
1179 Duke, and J. H. Porter. 2013. Big data and the future of ecology. *Frontiers in Ecology and the*
1180 *Environment* 11:156–162.
- 1181 Hansen, M. C., P. V. Potapov, R. Moore, M. Hancher, S. A. Turubanova, A. Tyukavina, D. Thau,
1182 S. V. Stehman, S. J. Goetz, T. R. Loveland, A. Kommareddy, A. Egorov, L. Chini, C. O. Justice,
1183 and J. R. G. Townshend. 2013. High-resolution global maps of 21st-century forest cover
1184 change. *Science* 342:850–853.
- 1185 Heffernan, J. B., P. A. Soranno, M. J. Angilletta, L. B. Buckley, D. S. Gruner, T. H. Keitt, J. R.
1186 Kellner, J. S. Kominoski, A. V. Rocha, J. Xiao, T. K. Harms, S. J. Goring, L. E. Koenig, W. H.
1187 McDowell, H. Powell, A. D. Richardson, C. A. Stow, R. Vargas, and K. C. Weathers. 2014.
1188 Macrosystems ecology: Understanding ecological patterns and processes at continental
1189 scales. *Frontiers in Ecology and the Environment* 12:5–14.
- 1190 Heidorn, P. B. 2008. Shedding Light on the Dark Data in the Long Tail of Science. *Library*
1191 *Trends* 57:280–299.
- 1192 Hijmans, R. J. 2021a. Terra: Spatial data analysis. manual.
- 1193 Hijmans, R. J. 2021b. Raster: Geographic data analysis and modeling. manual.
- 1194 Jackson, T. D., G. J. Williams, G. Walker-Springett, and A. J. Davies. 2020. Three-dimensional
1195 digital mapping of ecosystems: A new era in spatial ecology. *Proceedings of the Royal*
1196 *Society B: Biological Sciences* 287:20192383.

- 1197 James, M. R., and S. Robson. 2014. Mitigating systematic error in topographic models
1198 derived from UAV and ground-based image networks. *Earth Surface Processes and*
1199 *Landforms* 39:1413–1420.
- 1200 Joseph, M. B., A. Spiers, M. J. Koontz, N. Ilangakoon, K. Solvik, N. Quarderer, J. McGlinchy, V.
1201 Scholl, L. S. Denis, C. Nagy, A. Braswell, M. W. Rossi, L. Herwehe, L. Wasser, M. E. Cattau, V.
1202 Iglesias, A. L. Mahood, F. Yao, S. Leyk, and J. Balch. 2021. Ten simple rules for working with
1203 high resolution remote sensing data.
- 1204 Joseph, M., and L. Wasser. 2021. Neonhs: Work with NEON AOP hyperspectral data. manual.
- 1205 Joyce, K. E., K. Anderson, and R. E. Bartolo. 2021. Of course we fly unmanned– we’re
1206 women! *Drones* 5:21.
- 1207 Kampe, T. U., B. R. Johnson, M. A. Kuester, and M. Keller. 2010. NEON: The first continental-
1208 scale ecological observatory with airborne remote sensing of vegetation canopy
1209 biochemistry and structure. *Journal of Applied Remote Sensing* 4:043510.
- 1210 Karpowicz, B., and T. Kampe. 2015. NEON Imaging Spectrometer Radiance to Reflectance
1211 Algorithm Theoretical Basis Document. Page 47. National Ecological Observatory Network.
- 1212 Keller, M., D. S. Schimel, W. W. Hargrove, and F. M. Hoffman. 2008. A continental strategy
1213 for the National Ecological Observatory Network. *Frontiers in Ecology and the*
1214 *Environment* 6:282–284.
- 1215 Knapp, A. K., and C. D’Avanzo. 2010. Teaching with principles: Toward more effective
1216 pedagogy in ecology. *Ecosphere* 1:art15.

- 1217 Knyazikhin, Y., M. A. Schull, P. Stenberg, M. Möttus, M. Rautiainen, Y. Yang, A. Marshak, P. L.
- 1218 Carmona, R. K. Kaufmann, P. Lewis, M. I. Disney, V. Vanderbilt, A. B. Davis, F. Baret, S.
- 1219 Jacquemoud, A. Lyapustin, and R. B. Myneni. 2013. Hyperspectral remote sensing of foliar
- 1220 nitrogen content. *Proceedings of the National Academy of Sciences* 110:E185–E192.
- 1221 Koontz, M. J., A. M. Latimer, L. A. Mortenson, C. J. Fettig, and M. P. North. 2021. Cross-scale
- 1222 interaction of host tree size and climatic water deficit governs bark beetle-induced tree
- 1223 mortality. *Nature Communications* 12:129.
- 1224 Kuželka, K., and P. Surový. 2018. Mapping forest structure using UAS inside flight
- 1225 capabilities. *Sensors (Basel, Switzerland)* 18.
- 1226 LaRue, E. A., J. Rohr, J. Knott, W. K. Dodds, K. M. Dahlin, J. H. Thorp, J. S. Johnson, M. I. R.
- 1227 González, B. S. Hardiman, M. Keller, R. T. Fahey, J. W. Atkins, F. Tromboni, M. D.
- 1228 SanClements, G. Parker, J. Liu, and S. Fei. 2021. The evolution of macrosystems biology.
- 1229 *Frontiers in Ecology and the Environment* 19:11–19.
- 1230 Lawton, J. H. 1996. Patterns in Ecology. *Oikos* 75:145–147.
- 1231 Lehnert, L. W., H. Meyer, W. A. Obermeier, B. Silva, B. Regeling, and J. Bendix. 2019.
- 1232 Hyperspectral Data Analysis in R: The *hsdar* Package. *Journal of Statistical Software* 89:1–
- 1233 23.
- 1234 Leisso, N., T. Kampe, and B. Karpowicz. 2014. Calibration of the National Ecological
- 1235 Observatory Network's airborne imaging spectrometers. Pages 2625–2628 2014 IEEE
- 1236 Geoscience and Remote Sensing Symposium.

- 1237 Levin, S. A. 1992. The problem of pattern and scale in ecology: The Robert H. MacArthur
1238 award lecture. *Ecology* 73:1943–1967.
- 1239 Lindenmayer, D. F., and G. E. Likens. 2018. Maintaining the culture of ecology. *Frontiers in*
1240 *Ecology and the Environment* 16:195–195.
- 1241 Lunch, C., C. Laney, N. Mietkiewicz, E. Sokol, K. Cawley, and NEON (National Ecological
1242 Observatory Network). 2021. *neonUtilities: Utilities for working with NEON data.* manual.
- 1243 Miller, H. M. 2016. Users and uses of Landsat 8 satellite imagery survey results. Page 33.
1244 USGS Numbered Series, U.S. Geological Survey, Reston, VA.
- 1245 Miller, H. M., L. O. Serbina, L. A. Richardson, S. J. Ryker, and T. R. Newman. 2016. The Value
1246 of Earth Observations: Methods and Findings on the Value of Landsat Imagery. Pages 223–
1247 237 in J. L. Drake, Y. Y. Kontar, J. C. Eichelberger, T. S. Rupp, and K. M. Taylor, editors.
1248 Communicating Climate-Change and Natural Hazard Risk and Cultivating Resilience: Case
1249 Studies for a Multi-disciplinary Approach. Springer International Publishing, Cham.
- 1250 Nagaraj, A., E. Shears, and M. de Vaan. 2020. Improving data access democratizes and
1251 diversifies science. *Proceedings of the National Academy of Sciences* 117:23490–23498.
- 1252 Nagy, R. C., J. K. Balch, E. K. Bissell, M. E. Cattau, N. F. Glenn, B. S. Halpern, N. Ilangakoon, B.
1253 Johnson, M. B. Joseph, S. Marconi, C. O'Riordan, J. Sanovia, T. L. Swetnam, W. R. Travis, L. A.
1254 Wasser, E. Woolner, P. Zarnetske, M. Abdulrahim, J. Adler, G. Barnes, K. J. Bartowitz, R. E.
1255 Blake, S. P. Bombaci, J. Brun, J. D. Buchanan, K. D. Chadwick, M. S. Chapman, S. S. Chong, Y. A.
1256 Chung, J. R. Corman, J. Courret, E. Crispo, T. G. Doak, A. Donnelly, K. A. Duffy, K. H. Dunning, S.
1257 M. Duran, J. W. Edmonds, D. E. Fairbanks, A. J. Felton, C. R. Florian, D. Gann, M. Gebhardt, N.

- 1258 S. Gill, W. K. Gram, J. S. Guo, B. J. Harvey, K. R. Hayes, M. R. Helmus, R. T. Hensley, K. L.
1259 Hondula, T. Huang, W. J. Hundertmark, V. Iglesias, P.-A. Jacinthe, L. S. Jansen, M. A. Jarzyna,
1260 T. M. Johnson, K. D. Jones, M. A. Jones, M. G. Just, Y. O. Kaddoura, A. K. Kagawa-Vivani, A.
1261 Kaushik, A. B. Keller, K. B. S. King, J. Kitzes, M. J. Koontz, P. V. Kouba, W.-Y. Kwan, J. M.
1262 LaMontagne, E. A. LaRue, D. Li, B. Li, Y. Lin, D. Liptzin, W. A. Long, A. L. Mahood, S. S. Malloy,
1263 S. L. Malone, J. M. McGlinchy, C. L. Meier, B. A. Melbourne, N. Mietkiewicz, J. T. Morisette, M.
1264 Moustapha, C. Muscarella, J. Musinsky, R. Muthukrishnan, K. Naithani, M. Neely, K. Norman,
1265 S. M. Parker, M. Perez Rocha, L. Petri, C. A. Ramey, S. Record, M. W. Rossi, M. SanClements, V.
1266 M. Scholl, A. K. Schweiger, B. Seyednasrollah, D. Sihi, K. R. Smith, E. R. Sokol, S. A. Spaulding,
1267 A. I. Spiers, L. A. St. Denis, A. P. Staccone, K. Stack Whitney, D. M. Stanitski, E. Stricker, T. D.
1268 Surasinghe, S. K. Thomsen, P. M. Vasek, L. Xiaolu, D. Yang, R. Yu, K. M. Yule, and K. Zhu.
1269 2021. Harnessing the NEON data revolution to advance open environmental science with a
1270 diverse and data-capable community. *Ecosphere* 12:e03833.
- 1271 National Ecological Observatory Network. 2020. geoNEON: Geolocation data access for
1272 NEON data. manual.
- 1273 Nesbit, P. R., and C. H. Hugenholtz. 2019. Enhancing UAV model accuracy in high-relief
1274 landscapes by incorporating oblique images. *Remote Sensing* 11:239.
- 1275 Ni, W., G. Sun, Y. Pang, Z. Zhang, J. Liu, A. Yang, Y. Wang, and D. Zhang. 2018. Mapping three-
1276 dimensional structures of forest canopy using UAV stereo imagery: Evaluating impacts of
1277 forward overlaps and image resolutions with LiDAR data as reference. *IEEE Journal of*
1278 *Selected Topics in Applied Earth Observations and Remote Sensing* 11:3578–3589.

- 1279 NSF. 2013, April 18. National Ecological Observatory Network (NEON): Revolutionizing
1280 Ecological Research. https://www.nsf.gov/publications/pub_summ.jsp?ods_key=nsf13088.
- 1281 Olah, C., and S. Carter. 2017. Research debt. Distill 2:e5.
- 1282 Over, J.-S. R., A. C. Ritchie, C. J. Kranenburg, J. A. Brown, D. Buscombe, T. Noble, C. R.
1283 Sherwood, J. A. Warrick, and P. A. Wernette. 2021. Processing Coastal Imagery With Agisoft
1284 Metashape Professional Edition, Version 1.6 Structure From Motion Workflow
1285 Documentation. Page 46. Open-File Report, U.S. Geological Survey.
- 1286 Pádua, L., J. Vanko, J. Hruška, T. Adão, J. J. Sousa, E. Peres, and R. Morais. 2017. UAS, sensors,
1287 and data processing in agroforestry: A review towards practical applications. International
1288 Journal of Remote Sensing:1–43.
- 1289 Pebesma, E. 2018. Simple features for R: Standardized support for spatial vector data. The
1290 R Journal 10:439–446.
- 1291 Picotte, J. J., K. Bhattacharai, D. Howard, J. Lecker, J. Epting, B. Quayle, N. Benson, and K. Nelson.
1292 2020. Changes to the Monitoring Trends in Burn Severity program mapping production
1293 procedures and data products. Fire Ecology 16:16.
- 1294 Piermattei, L., W. Karel, D. Wang, M. Wieser, M. Mokroš, P. Surový, M. Koreň, J. Tomaštík, N.
1295 Pfeifer, and M. Hollaus. 2019. Terrestrial structure from motion photogrammetry for
1296 deriving forest inventory data. Remote Sensing 11:950.
- 1297 Plowright, A., and J.-R. Roussel. 2021. ForestTools: Analyzing remotely sensed forest data.
1298 manual.

- 1299 Popescu, S. C., and R. H. Wynne. 2004. Seeing the trees in the forest: Using LiDAR and
1300 multispectral data fusion with local filtering and variable window size for estimating tree
1301 height. *Photogrammetric Engineering and Remote Sensing*:16.
- 1302 R Core Team. 2021. R: A language and environment for statistical computing. manual, R
1303 Foundation for Statistical Computing, Vienna, Austria.
- 1304 Rosas, J. T. F., F. de A. de C. Pinto, D. M. de Queiroz, F. M. de M. Villar, R. N. Martins, and S. de
1305 A. Silva. 2020. Low-cost system for radiometric calibration of UAV-based multispectral
1306 imagery. *Journal of Spatial Science* 0:1–15.
- 1307 Rouse, W., R. H. Haas, W. Deering, and J. A. Schell. 1973. Monitoring the vernal advancement
1308 and retrogradation (green wave effect) of natural vegetation. Type II Report, Goddard
1309 Space Flight Center, Greenbelt, MD, USA.
- 1310 Roussel, J.-R., and D. Auty. 2021. Airborne LiDAR data manipulation and visualization for
1311 forestry applications. manual.
- 1312 Ruggiero, P., and M. A. Heckathorn. 2012. Data backup options. Page 6. United States
1313 Computer Emergency Response Team.
- 1314 Santana, L. S., G. A. E. S. Ferraz, D. B. Marin, B. D. S. Barbosa, L. M. D. Santos, P. F. P. Ferraz, L.
1315 Conti, S. Camiciottoli, and G. Rossi. 2021. Influence of flight altitude and control points in
1316 the georeferencing of images obtained by unmanned aerial vehicle. *European Journal of*
1317 *Remote Sensing* 54:59–71.
- 1318 Schimel, D. S. 2013. NEON Observatory Design. Pages 1–83. National Ecological
1319 Observatory Network.

- 1320 Scholl, V. M., M. E. Cattau, M. B. Joseph, and J. K. Balch. 2020. Integrating National Ecological
1321 Observatory Network (NEON) airborne remote sensing and in-situ data for optimal tree
1322 species classification. *Remote Sensing* 12:1414.
- 1323 Scholl, V. M., and A. M. Ku. 2021. Spectral reflectance measurements of radiometric
1324 calibration panels for UAS image calibration. U.S. Geological Survey.
- 1325 Smith, G. M., and E. J. Milton. 1999. The use of the empirical line method to calibrate
1326 remotely sensed data to reflectance. *International Journal of Remote Sensing* 20:2653–
1327 2662.
- 1328 Swayze, N. C., W. T. Tinkham, J. C. Vogeler, and A. T. Hudak. 2021. Influence of flight
1329 parameters on UAS-based monitoring of tree height, diameter, and density. *Remote Sensing*
1330 of Environment 263:112540.
- 1331 Swetnam, T. L., J. K. Gillan, T. T. Sankey, M. P. McClaran, M. H. Nichols, P. Heilman, and J.
1332 McVay. 2018. Considerations for Achieving Cross-Platform Point Cloud Data Fusion across
1333 Different Dryland Ecosystem Structural States. *Frontiers in Plant Science* 8.
- 1334 Tinkham, W. T., and N. C. Swayze. 2021. Influence of Agisoft Metashape parameters on UAS
1335 Structure from Motion individual tree detection from canopy height models. *Forests*
1336 12:250.
- 1337 Torres-Sánchez, J., F. López-Granados, I. Borra-Serrano, and J. M. Peña. 2018. Assessing
1338 UAV-collected image overlap influence on computation time and digital surface model
1339 accuracy in olive orchards. *Precision Agriculture* 19:115–133.

- 1340 Turner, M. G. 1989. Landscape ecology: The effect of pattern on process. *Annual Review of
1341 Ecology and Systematics* 20:171–197.
- 1342 Vincent, J. B., L. K. Werden, and M. A. Ditmer. 2015. Barriers to adding UAVs to the
1343 ecologist's toolbox. *Frontiers in Ecology and the Environment* 13:74–75.
- 1344 Wang, C., and S. W. Myint. 2015. A Simplified Empirical Line Method of Radiometric
1345 Calibration for Small Unmanned Aircraft Systems-Based Remote Sensing. *IEEE Journal of
1346 Selected Topics in Applied Earth Observations and Remote Sensing* 8:1876–1885.
- 1347 Wang, Z., A. Chlus, R. Geygan, Z. Ye, T. Zheng, A. Singh, J. J. Couture, J. Cavender-Bares, E. L.
1348 Kruger, and P. A. Townsend. 2020. Foliar functional traits from imaging spectroscopy
1349 across biomes in eastern North America. *New Phytologist* 228:494–511.
- 1350 Weinstein, B. G., S. J. Graves, S. Marconi, A. Singh, A. Zare, D. Stewart, S. A. Bohlman, and E. P.
1351 White. 2021. A benchmark dataset for canopy crown detection and delineation in co-
1352 registered airborne RGB, LiDAR and hyperspectral imagery from the National Ecological
1353 Observation Network. *PLOS Computational Biology* 17:e1009180.
- 1354 Weinstein, B. G., S. Marconi, S. A. Bohlman, A. Zare, and E. P. White. 2020. Cross-site
1355 learning in deep learning RGB tree crown detection. *Ecological Informatics* 56:101061.
- 1356 Weinstein, B. G., S. Marconi, S. Bohlman, A. Zare, and E. White. 2019. Individual tree-crown
1357 detection in RGB imagery using semi-supervised deep learning neural networks. *Remote
1358 Sensing* 11:1309.

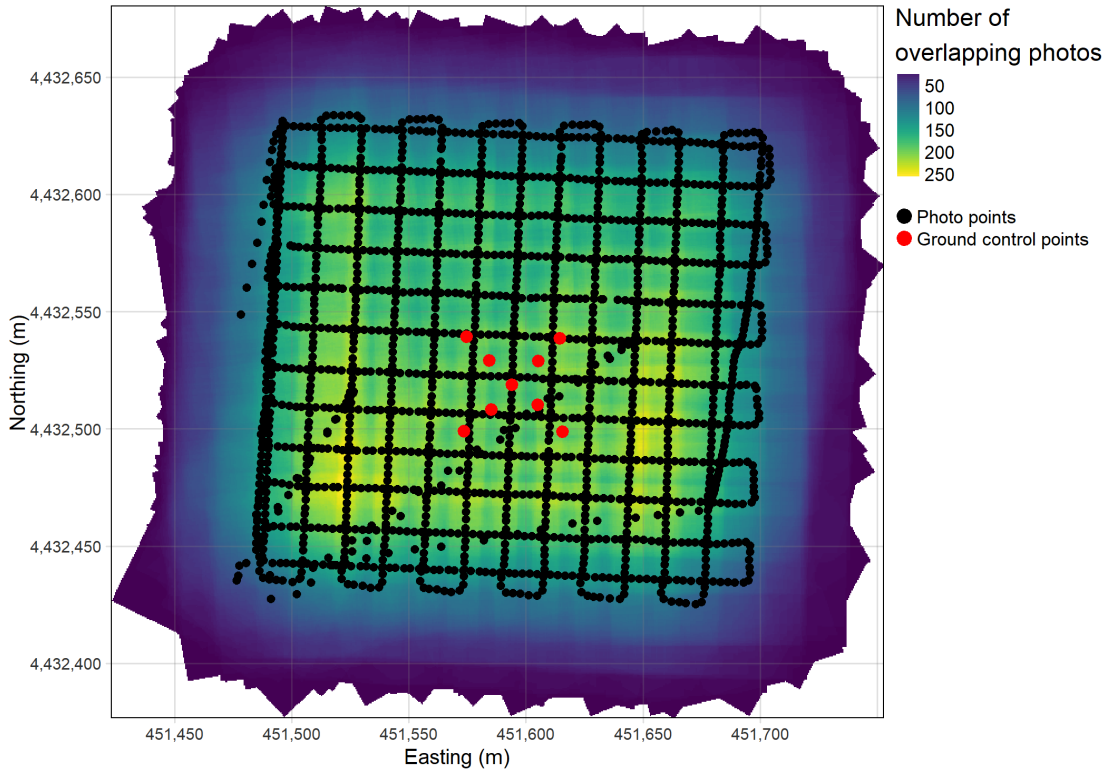
- 1359 Westoby, M. J., J. Brasington, N. F. Glasser, M. J. Hambrey, and J. M. Reynolds. 2012.
- 1360 'Structure-from-Motion' photogrammetry: A low-cost, effective tool for geoscience
- 1361 applications. *Geomorphology* 179:300–314.
- 1362 Wyngaard, J., L. Barbieri, A. Thomer, J. Adams, D. Sullivan, C. Crosby, C. Parr, J. Klump, S. Raj
- 1363 Shrestha, and T. Bell. 2019. Emergent challenges for science sUAS data management:
- 1364 Fairness through community engagement and best practices development. *Remote Sensing*
- 1365 11:1797.
- 1366 Young, D. J. N., M. J. Koontz, and J. Weeks. 2021. Optimizing aerial imagery collection and
- 1367 processing parameters for drone-based individual tree mapping in structurally complex
- 1368 conifer forests.
- 1369 Zhang, W., J. Qi, P. Wan, H. Wang, D. Xie, X. Wang, and G. Yan. 2016. An easy-to-use airborne
- 1370 LiDAR data filtering method based on cloth simulation. *Remote Sensing* 8:501.
- 1371 Zimmerman, T., K. Jansen, and J. Miller. 2020. Analysis of UAS flight altitude and ground
- 1372 control point parameters on DEM accuracy along a complex, developed coastline. *Remote*
- 1373 *Sensing* 12:2305.
- 1374 Zipkin, E. F., E. R. Zylstra, A. D. Wright, S. P. Saunders, A. O. Finley, M. C. Dietze, M. S. Itter,
- 1375 and M. W. Tingley. 2021. Addressing data integration challenges to link ecological
- 1376 processes across scales. *Frontiers in Ecology and the Environment* 19:30–38.

1377 **Tables**1378 *Table 1: Summary of vehicle and payload considerations for UAS-enabled ecology.*

Consideration	Options	Advantages	Disadvantages	Reference(s)
Vehicle	Rotocopter	Ease of takeoff and landing	Shorter flight time (~20 minutes)	Anderson and Gaston (2013); Goodbody et al. (2017); Pádua et al. (2017)
		Hover capability		
		Maneuverability		
		Affordable		
	Fixed wing	Longer flight time (2+ hours)	Higher minimum flight speed to keep it aloft (affecting overlap, image quality)	
		Covers large spatial extent	Complex takeoff/landing	
		More stable in wind		
	VTOL fixed wing hybrid	Simpler takeoff/landing	Newer technology	
		Longer flight time	Expensive	
Payload	RGB camera	Small size	Limited spectral extent to visible wavelengths	Pádua et al. (2017); Adão et al. (2017)
		Affordable	Spectrally overlapping, imprecise spectral information	
		Fine spatial resolution		

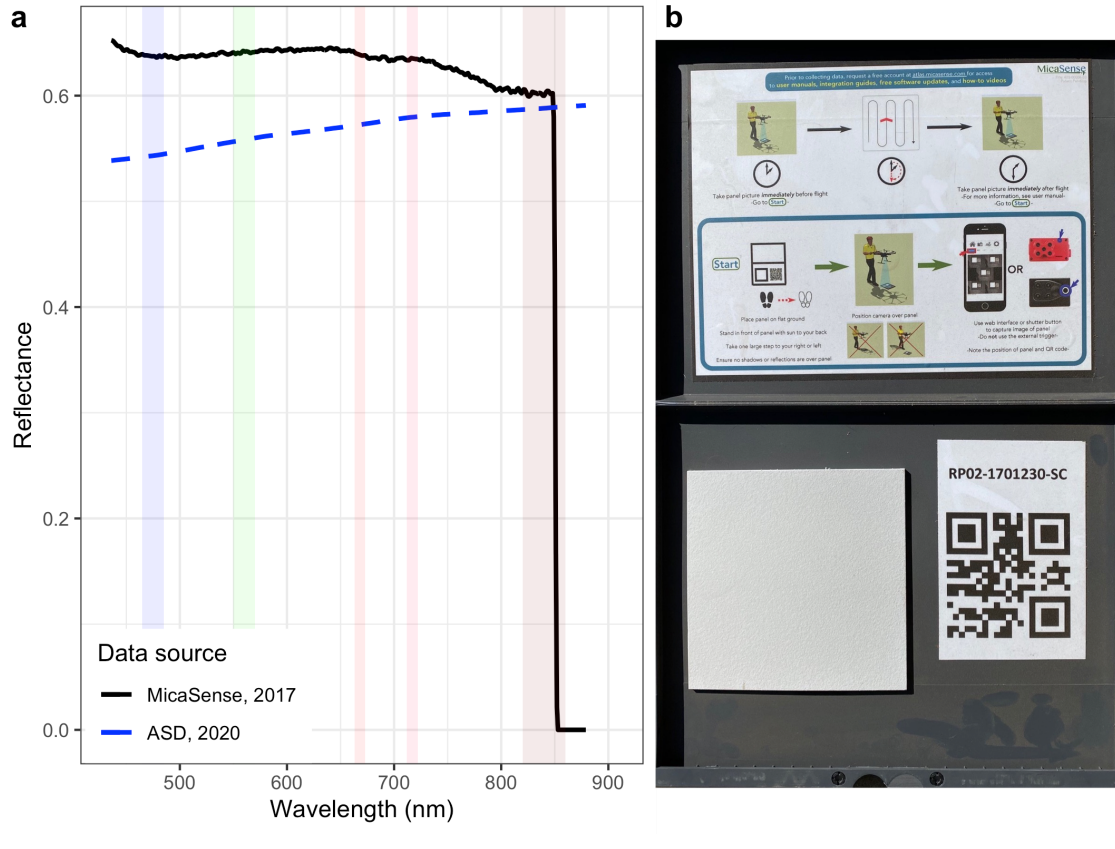
Multispectral sensor	Small size	Limited spectral sampling typically in visible and infrared wavelengths
	More precise spectral information	More complex data acquisition and post-processing
Hyperspectral/Imaging spectrometer	High spectral resolution	Heavy
	High spectral extent	Expensive
		Very complex data acquisition and post-processing

1379 **Figure legends**



1380

1381 *Figure 1: Black points depict the UAS position for each photo captured during the flight. Red*
1382 *points in the "X" formation at the center are the high-precision geolocations of the NEON*
1383 *vegetation plot monuments. The background color represents the approximate number of*
1384 *photos captured over each point in the surveyed area based on idealized image footprints*
1385 *projected on the ground surrounding the geolocation of each photo point (i.e., the black*
1386 *points). Each point needs to be imaged a large number of times (likely more than 100 for*
1387 *denser vegetation), which means that some areas with image capture at the edges of the*
1388 *flew area won't have coverage suitable for structure from motion data processing. The flight*
1389 *area should therefore be larger than the area of interest to ensure sufficient data coverage.*



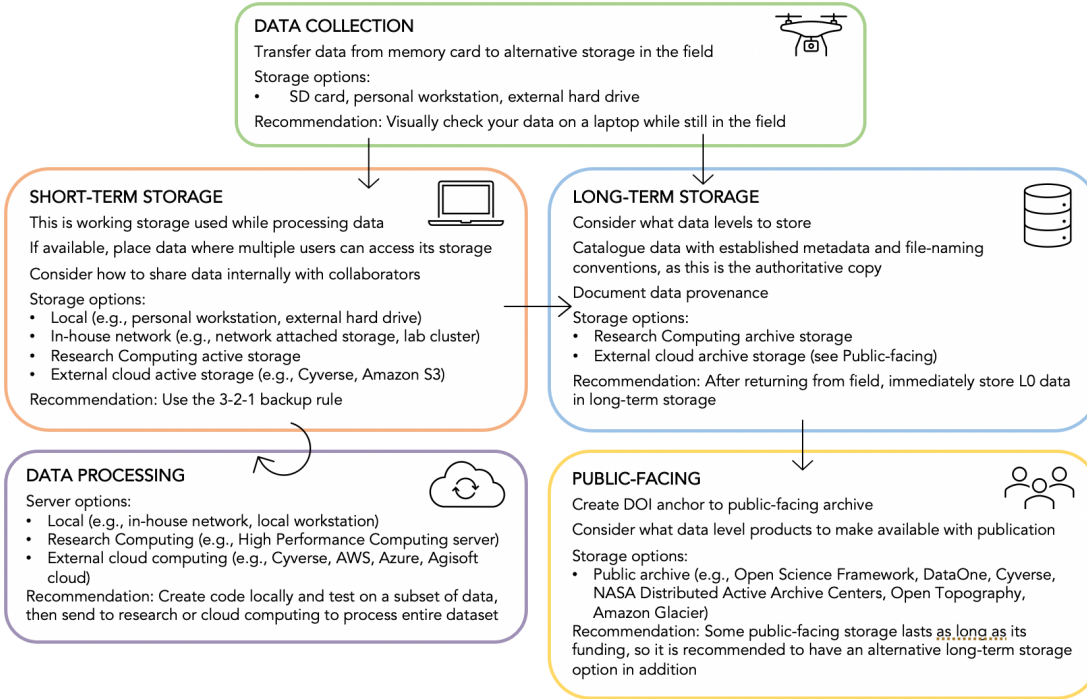
1390 *Figure 2: a) Reflectance of a calibrated reflectance panel as a function of wavelength. The
 1391 black solid line corresponds to the manufacturer-provided reflectance spectrum representing
 1392 the panel's reflectance at the time of purchase. The blue dashed line corresponds to
 1393 remeasurements of the panel's reflectance spectrum in 2020 with a handheld spectrometer,
 1394 after three years of field use. The MicaSense RedEdge 3 spectral band ranges (blue, green, red,
 1395 red edge, near infrared) are depicted as vertical bars of color. The panel reflectance decreased
 1396 between 2017 and 2020, with this decrease being more pronounced towards the shorter
 1397 wavelengths. b) A photograph of the calibrated reflectance panel measured in a), taken in
 1398 2020 after three years of field use. The change in reflectance between 2017 and 2020 is likely
 1399 the result of accumulated dust and sand from the field, as seen partially wiped away on the
 1400 lower, right corner of the panel's plastic case. The difference between the manufacturer-*

1402 reported panel reflectance and the actual reflectance after heavy use demonstrates the
1403 necessity to clean, remeasure, or replace calibration panels when performing radiometric
1404 calibration.



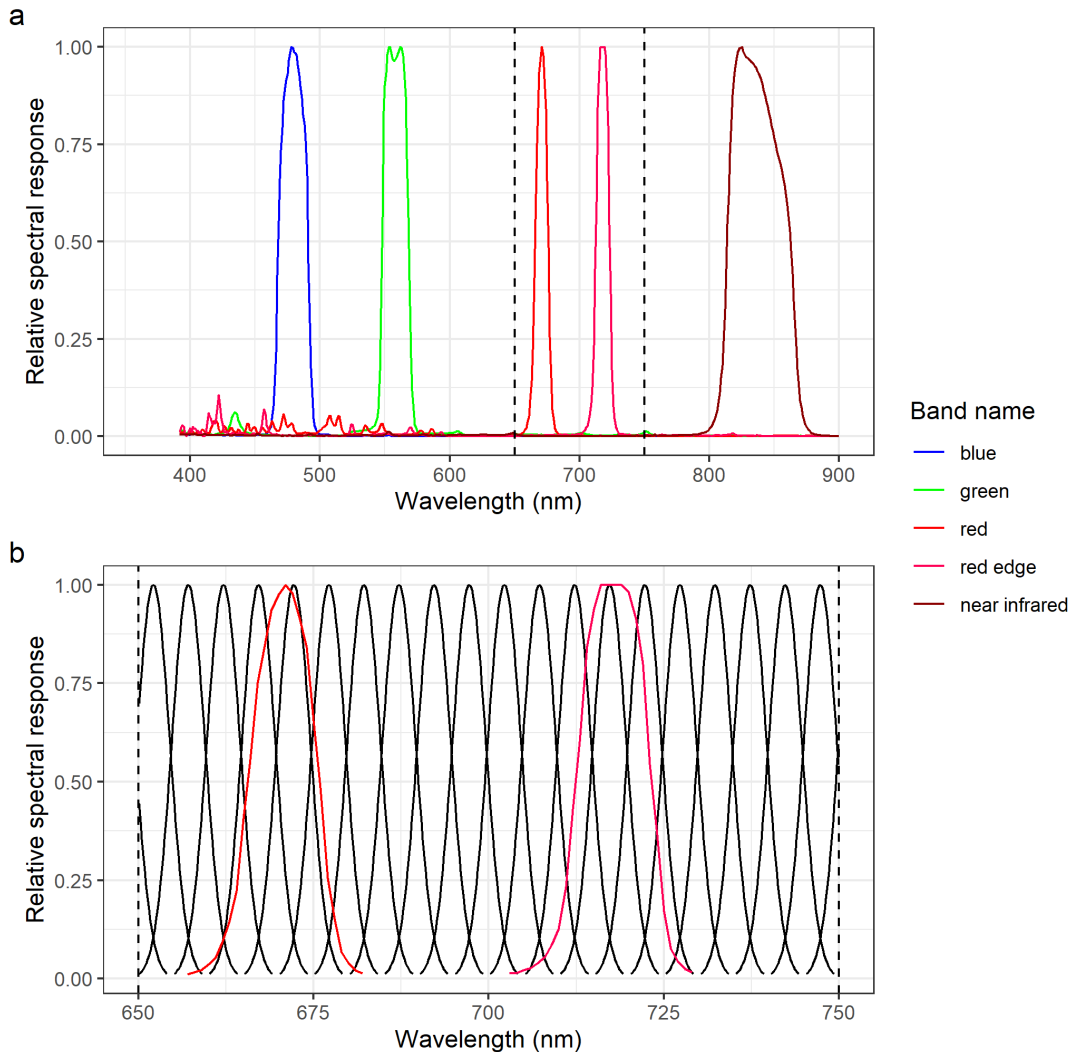
1405

1406 *Figure 3: Aerial RGB photograph captured using a DJI Phantom 4 Pro on January 23, 2020 at*
1407 *120m of altitude above ground level. The photo depicts three ground control points (GCPs)*
1408 *each of two different types in the center of the image: 1 m long spray painted orange cotton*
1409 *drop cloth in an "X" pattern and 1 x 1 m squares of cotton drop cloth spray painted with black*
1410 *triangles. The GCPs are progressively more conspicuous under the canopy, in the shrub field,*
1411 *and on the dirt road. The size of the area covered by the main photograph is approximately*
1412 *180 m wide x 120 m high.*



1413

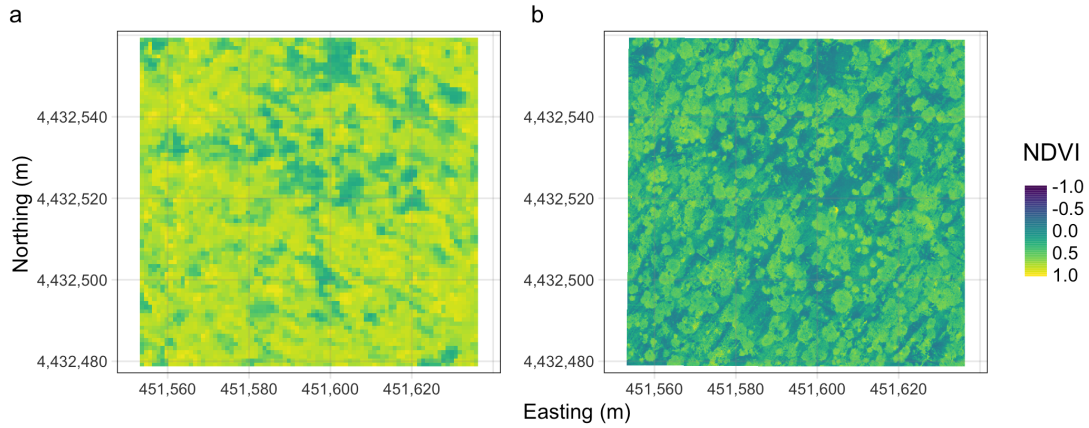
1414 *Figure 4: Planning a data management pipeline is a large upfront investment but can save*
 1415 *time and money in the long-run, making it well-worth prioritizing up-front. Considering the*
 1416 *storage, backup, and sharing needs of the datasets you anticipate collecting and processing*
 1417 *ensure data persistency and availability. This data pipeline describes options and includes*
 1418 *recommendations. There are trade-offs at each decision point, so it is important to*
 1419 *understand your data needs and budget. For example, whereas building your own data*
 1420 *management system may be more affordable and tailored to your needs, rented external*
 1421 *storage systems will back up your data automatically and maintain the system and hardware*
 1422 *requirements for you.*



1423

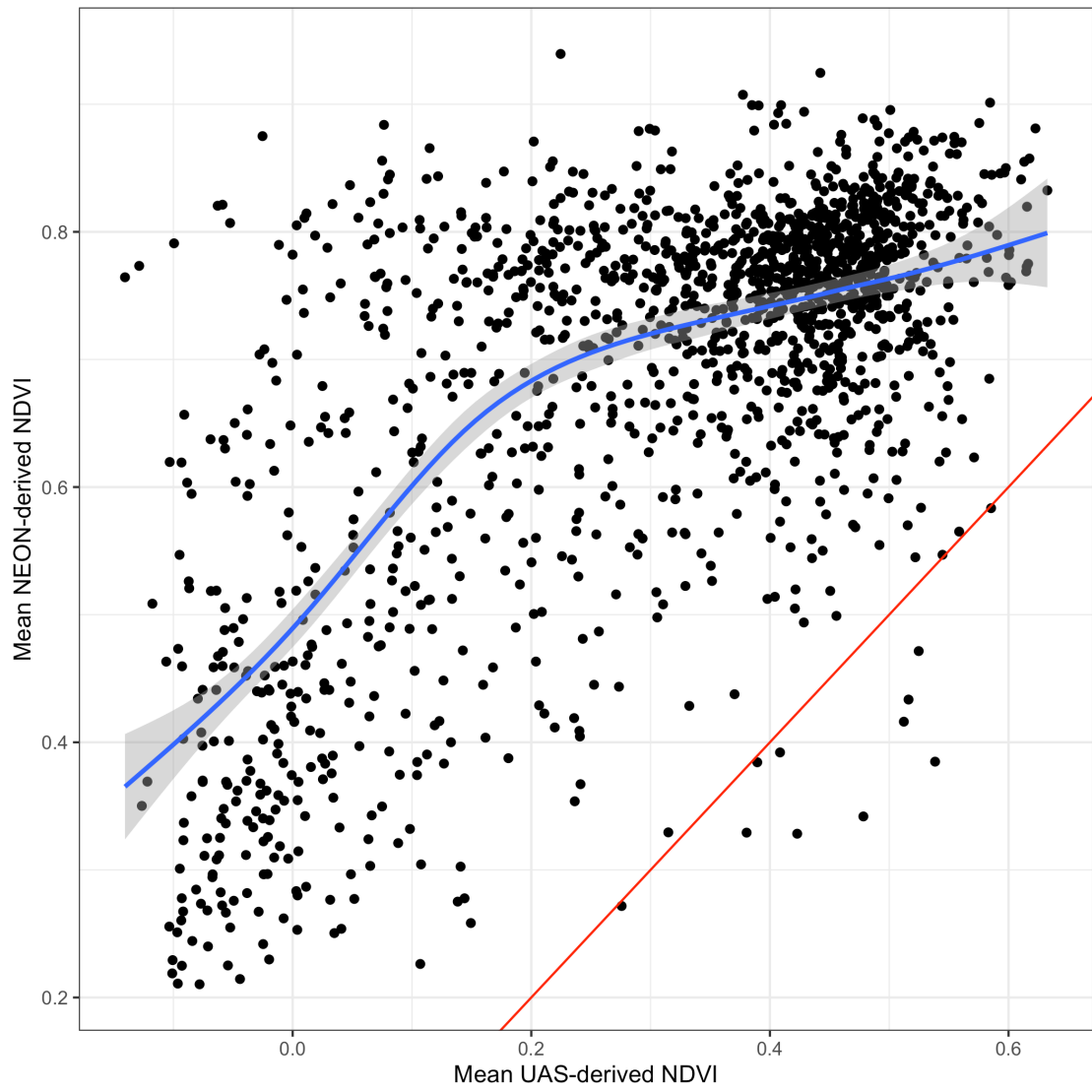
1424 *Figure 5: a) Relative spectral response of the MicaSense RedEdge 3 camera in 5 distinct*
 1425 *spectral bands based on the quantum efficiency of the image sensor per wavelength and the*
 1426 *bandpass filter transmission per wavelength. The dashed vertical lines in a) demarcate the*
 1427 *spectral extent of panel b). b) Relative spectral responses for two channels of the MicaSense*
 1428 *RedEdge 3 camera plotted with the relative spectral responses for twenty channels of the*
 1429 *NEON AOP imaging spectrometer. Several channels of the NEON AOP instrument comprise*
 1430 *each of the MicaSense RedEdge 3 channels, so the reflectance data from the NEON AOP are*

1431 resampled (weighted, in effect) such that they can be used as though the NEON instrument
1432 exhibited the same spectral sensitivity as the MicaSense RedEdge 3 instrument.



1433

1434 *Figure 6: NDVI image over NIW0017 plot a) derived from the NEON AOP spectral imager*
1435 *using data collected in August of 2019 (data collection flights over NIWO on August 14, 15, 19,*
1436 *and 26 of 2019) and b) derived from the MicaSense RedEdge 3 camera using data collected on*
1437 *October 09, 2019. The NEON AOP data were first spectrally resampled into the equivalent red*
1438 *and near infrared bands of the MicaSense RedEdge 3 camera based on the relative spectral*
1439 *response of the RedEdge 3 instrument. The higher spatial resolution of the drone-derived data*
1440 *are highlighted. Note that the difference in NDVI between the images may derive from three*
1441 *main sources: phenological differences in the vegetation, differences in the flight conditions*
1442 *such as time of day and cloud cover, or differences in instrumentation.*



1443

1444 *Figure 7: NDVI for each detected tree crown in the NIWO_017 plot as derived from the NEON*
 1445 *AOP imaging spectrometer versus NDVI derived from the MicaSense RedEdge 3 sensor. The*
 1446 *one-to-one line is red, and the best fit curve from a general additive model is shown in blue*
 1447 *with a 95% confidence interval shown in gray. The NEON AOP data, collected closer to peak*
 1448 *growing season, mostly has higher per-tree values of NDVI. The nonlinear model fit highlights*
 1449 *how, at the individual tree scale, spectral responses vary differently throughout the year*

1450 *which might prove useful for future work (e.g., classifying trees to species based on how*
1451 *variable their spectral response is through the year).*